Molecular Biology and Evolution, msab271, https://doi.org/10.1093/molbev/msab271
Accepted manuscript published 07 September 2021

Article Submission
Discoveries Section

Two functional epithelial sodium channel isoforms are present in rodents despite pronounced evolutionary pseudogenisation and exon fusion

Sean M. Gettings[1,2*], Stephan Maxeiner[3*], Maria Tzika[1], Matthew R. D. Cobain[1], Irina Ruf[4], Fritz Benseler[5], Nils Brose[5], Gabriela Krasteva-Christ[3], Greetje Vande Velde[2], Matthias Schönberger[2§] and Mike Althaus[6#]

[1] School of Natural and Environmental Sciences, Newcastle University, Newcastle upon Tyne, United Kingdom
[2] Biomedical Imaging, Department of Imaging and Pathology, Faculty of Medicine, KU Leuven, Belgium
[3] Institute for Anatomy and Cell Biology, Saarland University School of Medicine, Homburg, Germany
[4] Division of Messel Research and Mammalogy, Senckenberg Research Institute and Natural History Museum Frankfurt, Frankfurt am Main, Germany
[5] Department of Molecular Neurobiology, Max Planck Institute of Experimental Medicine, Göttingen, Germany
[6] Institute for Functional Gene Analytics, Department of Natural Sciences, Bonn-Rhein-Sieg University of Applied Sciences, Rheinbach, Germany

* These authors contributed equally to this study. Authors appear in alphabetical order.
§ Affiliation at the time of the project start.

[#] Correspondence: Prof. Dr. Mike Althaus
Institute for Functional Gene Analytics
Department of Natural Sciences
Bonn-Rhein-Sieg University of Applied Sciences
Von-Liebig-Strasse 20
53359 Rheinbach, Germany

Email: mike.althaus@h-brs.de

Abstract

The epithelial sodium channel (ENaC) plays a key role in salt and water homeostasis in tetrapod vertebrates. There are four ENaC subunits (α, β, γ, δ), forming heterotrimeric αβγ- or δβγ-ENaCs. While the physiology of αβγ-ENaC is well understood, for decades the field has stalled with respect to δβγ-ENaC due to the lack of mammalian model organisms. The *SCNN1D* gene coding for δ-ENaC was previously believed to be absent in rodents, hindering studies using standard laboratory animals. We analysed all currently available rodent genomes and discovered that *SCNN1D* is present in rodents but was independently lost in five rodent lineages, including the Muridae (mice and rats). The independent loss of *SCNN1D* in rodent lineages may be constrained by phylogeny and taxon-specific adaptation to dry habitats, however habitat aridity does not provide a selection pressure for maintenance of *SCNN1D* across Rodentia. A fusion of two exons coding for a structurally flexible region in the extracellular domain of δ-ENaC appeared in the Hystricognathi (a group that includes guinea pigs). This conserved pattern evolved at least 41 Ma ago and represents a new autapomorphic feature for this clade. Exon fusion does not impair functionality of guinea pig (*Cavia porcellus*) δβγ-ENaC expressed in *Xenopus* oocytes. Electrophysiological characterisation at the whole-cell and single-channel level revealed conserved biophysical features and mechanisms controlling guinea pig αβγ- and δβγ-ENaC function as compared to human orthologues. Guinea pigs therefore represent commercially available mammalian model animals that will help shed light on the physiological function of δ-ENaC.

Keywords: epithelial sodium channel, ENaC, rodent, evolution, delta-subunit, *SCNN1D*, pseudogene, exon fusion

Introduction

Water-to-land transition in the Devonian period, a key event in the evolution of tetrapod vertebrates (Daeschler et al. 2006), required significant physiological adaptations, including efficient mechanisms of sodium and water homeostasis which involve complex transport mechanisms in vertebrate kidneys (Kuo and Ehrlich. 2012; Rossier et al. 2015). In tetrapod vertebrates, sodium and water balance is controlled by hormones that match dietary sodium and water intake to their excretion rates. Vasopressin controls aquaporin-mediated renal water re-absorption and the renin-angiotensin-aldosterone system (RAAS) fine-tunes renal sodium re-absorption via epithelial sodium channels (ENaCs) (Rossier et al. 2015).

The canonical ENaC found in mammalian renal distal convoluted tubules and the cortical collecting ducts is composed of three homologous subunits (α, β, γ) which assemble into a heterotrimeric, sodium-selective ion channel (Noreng et al. 2018). ENaCs are constitutively active ion channels, but channel activity can be adjusted by a multitude of regulatory mechanisms and stimuli (Kleyman and Eaton 2020). Whereas hormones such as aldosterone control ENaC subunit expression (Rossier et al. 2015), the abundance of ENaCs in the plasma membrane is controlled by a complex intracellular signalling network that regulates trafficking to and removal from the plasma membrane (Baines 2013). Furthermore, ENaC open probability is affected by the extracellular sodium and proton concentration (Kashlan et al. 2015; Wichmann et al. 2019; Kleyman and Eaton 2020), processing by intra- and extracellular proteases (Kleyman and Eaton 2020), and mechanical stimuli (Althaus et al. 2007; Knoepp et al. 2020). The importance of a precise adjustment of ENaC activity is illustrated by ENaC mutations that lead to severe human diseases. Mutations that result in enhanced (αβγ-) ENaC activity cause Liddle syndrome (Shimkets et al. 1994), a hereditary form of hypertension, whereas mutations reducing ENaC activity cause hypotension and severe salt-wasting (pseudohypoaldosteronism type 1) (Chang et al. 1996).

Three genes coding for α-, β- and γ-ENaC (*SCNN1A*, *SCNN1B* and *SCNN1G*, respectively) are present in modern cyclostomes, indicating that ENaC evolved early in vertebrates and likely became part of a machinery that controlled sodium homeostasis when vertebrates migrated to freshwater and terrestrial environments (Hanukoglu and Hanukoglu 2016; Wichmann and Althaus 2020). A fourth ENaC subunit (δ), which is homologous to the α-subunit, appears in lobe-finned fishes (sarcopterygians) and is present in all major tetrapod lineages (Wichmann and Althaus 2020).

Functional characterisation of human and amphibian ENaC orthologues revealed that the δ-subunit can form heteromeric channels with the β- and γ-subunits (Waldmann et al. 1995; Babini et al. 2003). Interestingly, the presence of the δ-subunit changes the biophysical properties and molecular regulation of the channel. Compared to αβγ-ENaCs, δβγ-ENaCs

have an enhanced activity generating larger ion currents in heterologous expression systems (Haerteis et al. 2009; Wichmann et al. 2018). Several regulatory mechanisms controlling ENaC activity, such as the auto-regulatory control by extracellular sodium ions (a processes termed sodium self-inhibition, SSI), the sensitivity to the extracellular pH, channel processing by proteases, or response to mechanical stimuli, differs between δβγ-ENaCs and αβγ-ENaCs (Haerteis et al. 2009; Wichmann et al. 2018; Wichmann et al. 2019; Knoepp et al. 2020). However, the physiological function of the δ-subunit remains unknown, and it is unclear whether it evolved as an additional level of ENaC regulation in tetrapod vertebrates or resembles an evolutionary relic of an α-subunit-like ancestor (Wichmann and Althaus 2020).

Despite intensive efforts to elucidate the physiological function of δ-ENaC, to the best of our knowledge, no study up to today has reported a direct functional detection of δ-ENaC current signals *in vivo*. This is due to the lack of appropriate pharmacological tools to discriminate between αβγ- and δβγ-ENaCs, and lack of suitable model organisms (Paudel et al. 2021). Major advances in understanding the physiology and pathophysiology of canonical αβγ-ENaC were made by manipulating the genes encoding these three ENaC-subunits in mice. Unfortunately, the gene encoding the δ-subunit (*SCNN1D*) is believed to be a pseudogene in rodents, thus limiting research using the most common animal models in physiology and biomedicine. Consistently, Paudel et al. (2021) recently highlighted the need for appropriate rodent animal models in order to shed light on the role of δ-ENaC in health and disease. Apart from their important role as animal models in biomedical research, rodents comprise approximately 40 % of all extant mammalian species (Burgin et al. 2018). The order Rodentia is characterised by striking adaptive and evolutionary radiations, resulting in great diversity, e.g., in terms of locomotion, diet, geographical distribution, and ecology (Fabre et al. 2012; Cox and Hautier 2015). Rodents are therefore suitable model organisms for diverse research areas.

To study the enigmatic ENaC δ-subunit in rodents, we examined the existence of functional *SCNN1D* genes in the currently sequenced rodent genomes. First, we found that the *SCNN1D* gene it is not generally absent in rodents but was independently lost in different rodent suborders, including mice and rats. Second, we observed the fusion of two exons and incorporation of intron DNA into the δ-ENaC coding sequence in the Hystricomorpha (a group that includes guinea pigs). Third, we demonstrate that this exon fusion affects a structurally flexible region of the ion channel and does not impair functionality of guinea pig (*Cavia porcellus*) ENaCs in heterologous expression systems. Fourth, we provide evidence for conserved regulatory characteristics of guinea pig αβγ- and δβγ-ENaCs as compared to human orthologues and identify new molecular characteristics that indicate a physiological role in sodium homeostasis. Finally, we aimed to identify patterns in the geographical distribution

of rodent species that maintained or lost their functional δ-ENaC in order to shed light on the lack of potential selection pressures resulting in pseudogenisation of *SCNN1D*.

Results

Standardising* SCNN1 *gene nomenclature. To categorise the characteristics common to all four *SCNN1* genes and the particular differences that we observed regarding the evolution of *SCNN1D*, and to facilitate future comparisons, we propose a standardisation of the nomenclature for the exons of all *SCNN1* genes. Alternative splicing within the 'core' coding regions of all *SCNN1* genes, i.e., the sequence encompassing both transmembrane regions and, hence, the entire extracellular part, has not yet been reported. Consistent with Saxena et al. (1998), the first transmembrane coding exon should therefore be defined as 'exon 2', and all downstream exons numerated accordingly, concluding with exon 13 (Figure 1 A). Exon 13 encodes the second transmembrane region and the entire C-terminus. It appears that most but not all translational initiation sites are encoded by exon 2, with some being subject to alternative splicing of upstream exons, e.g. human *SCNN1D* which has 16 exons (Giraldez et al. 2012; Wesch et al. 2012; Zhao et al. 2012). To include potential translational start sites encoded by additional and/or alternative start sites upstream of exon 2, we suggest referring to those regions that contain experimentally validated start sites as exon 1. In the case of multiple exons upstream of exon 2, the exon 1 nomenclature should include alphabetical lettering, e.g., exon 1a, exon 1b, etc. This standardised nomenclature consistently aligns the coding regions in different exons (gene level) with the structural features (protein level) that have recently been resolved for human αβγ-ENaC (Figure 1 B and C). The extracellular loop of each ENaC subunit resembles a clenched hand holding a 'ball-like' structure (Figure 1 B) (Noreng et al. 2018). The 'finger' and 'thumb' are considered the major domains involved in ENaC gating, whereas the 'palm' and 'knuckle' domains contribute to channel regulation via inter-subunit interactions (Noreng et al. 2018). This conserved protein structure is also reflected in the organization of the *SCNN1* genes themselves. Exon 2 and 13 encode the transmembrane region, flanking exons 3 to 12 which encode the extracellular part.

Distribution of functional* SCNN1D *in rodents. The absence of *SCNN1D* in the genomic drafts of the rat and mouse genomes prompted us to search for potentially functional *SCNN1D* homologues in rodent genomes of different suborders, with the aim of determining whether *SCNN1D* is generally absent from rodents or specific to a subset thereof. This approach was further motivated by our earlier observation of selective erosion and gene loss within the pseudo-autosomal regions of Myomorpha genomes, which is not seen in other suborders (Maxeiner et al. 2020). Currently, 35 rodent families are recognised (D'Elía et al. 2019) (Figure 2), comprising three major clades: Hystricomorpha (a group that includes Old World

porcupines, chinchillas and guinea pigs), Sciuromorpha (squirrels, dormice and mountain beaver) and Supramyomorpha. The Supramyomorpha are divided into Anomaluromorphi (anomalures and springhares), Castorimorphi (beavers and kangaroo rats), and Myomorphi (mouse-like species) (D'Elía et al. 2019). We investigated the evolutionary fate of the *SCNN1D* gene in all currently available genome sequences within this diverse order (Table 1, Supplemental Spreadsheet) and made two major observations, a fusion of exons 11 and 12 to a 'super-exon' and an independent loss of the *SCNN1D* gene from all rodent suborders (including at least seven families). The generation of a super-exon is exclusive to the suborder Hystricomorpha, specifically to the infraorder Hystricognathi which includes guinea pigs (*Cavia porcellus*). Within the Sciuromorpha, two of the three families, Aplodontiidae (mountain beaver) and Gliridae (dormouse species), retain a functional *SCNN1D* copy, whereas it is absent from representatives of the Sciuridae family (the squirrel family). Sequence information on members of the Anomaluromorphi is limited but a potentially functional *SCNN1D* gene was found in the South African springhare (*Pedetes capensis*) which belongs to the Pedetidae family. In the Castorimorphi, a full *SCNN1D* reading frame was found in the American beaver (*Castor canadensis)*, belonging to the Castoridae, but there was no functional gene in the Gobi jerboa (*Allactata bullata*), illustrating the loss of *SCNN1D* in species within the Dipodidae family. The largest infraorder is the Myomorphi with the superfamilies Dipodoidea and Muroidea. Members of three out of five Muroidea families, the Muridae (rats, mice, gerbils), Cricetidae (hamsters, voles, lemmings, New World rats and mice) and Nesomyidae (Malagasy rats and mice and specific African species), retained only traces of an evolutionary ancient and, once likely, functional *SCNN1D* gene, which explains failed efforts to clone *SCNN1D* from laboratory mice, rats or hamsters. Bioinformatic evidence indicates that only the Spalacidae family (blind mole-rats) and the genus *Zapus* within the superfamily Dipodoidea potentially have a functional *SCNN1D* copy, whereas the genera *Jaculus* and *Allactaga* do not. In the Hystricomorpha, multiple stop codons were present in the *SCNN1D* gene of the Patagonian mara (*Dolichotis patagonum*), illustrating gene loss in genera within the Caviidae family, whereas guinea pigs (*C. porcellus*) retained intact open reading frames in *SCNN1D*. Despite the loss of functional *SCNN1D* from several of the families mentioned above, evidence of a decaying *SCNN1D* is still present, embedded between the flanking genes *ACAP3* and *UBE2J2,* which allowed us to integrate sequence information of exon 6 to plot a phylogenetic tree (Supplemental Figure 1, Supplemental Data 2, Supplemental Spreadsheet). An exception was the Heteromyidae in which *SCNN1D* is completely absent.

Analysis of four* SCNN1 *genes in the guinea pig. Analyses of the complete *SCNN1D* gene sequences of available rodent genomes revealed that guinea pigs retain a functional *SCNN1D* gene (Figure 2). Caviidae are an interesting rodent family in that the *SCNN1D* gene in this

family displays a fusion of exons 11 and 12 to a super-exon (including the incorporation of intron sequences) (Figure 3) while some family members (e.g., *D. patagonum*) lost a functional *SCNN1D*. We therefore explored whether the open reading frame of the guinea pig (*C. porcellus*) *SCNN1D* is indicative of a functional gene product, i.e., an ion channel with the functional characteristics of known ENaC orthologues (Haerteis et al. 2009; Giraldez et al. 2012; Wichmann et al. 2018).

We outlined the genomic structure of the *SCNN1* genes in *C. porcellus* and added experimental data for the presence of 'predicted' exons upstream of exon 2 based on our 5'RACE results. Given the reduced size of the entire *SCNN1D* gene and its anticipated high GC content (Table 2), we initially needed to validate the primary DNA sequence of the guinea pig *SCNN1D* gene (Gene ID: 100714892) in order to rule out high-throughput sequencing artifacts. Indeed, re-sequencing revealed a frame-shift in the very C-terminus. The corrected sequence has been deposited on GenBank (MN187539). *SCNN1A*, *SCNN1B* and *SCNN1G* have a generally similar gene organization (Hanukoglu and Hanukoglu 2016). The 5'RACE experiments revealed the inclusion of a single exon upstream of exon 2 for *SCNN1A* and *SCNN1B*, while in the case of *SCNN1G* two alternative exons are present (1a or 1b, Figure 3 A). The *SCNN1D* gene displays three major distinguishing features as compared to its homologues: (1) A collapsed gene size and increased GC content (Table 2, Figure 3 A, Supplemental Spreadsheet); (2) two alternative transcriptional start sites (short and long versions of exon 2) and the absence of any upstream exons, i.e., absence of exon 1; (3) a fusion of exon 11 and 12 forming a 'super-exon' (11*) due to the loss of splice donor and acceptor sites (Figure 3 A).

The amino acid sequence of guinea pig δ-ENaC was analysed in comparison with human δ-ENaC and the α-subunits of both species (Figure 3 B, Supplemental Data 2). Four major differences in key regulatory motifs were observed between the δ- and α-subunits: (1) A domain that is unique to ENaC, and referred to as the Gating Relief of Inhibition by Proteolysis (GRIP) domain (Figure 1 C) (Noreng et al. 2018), is shorter in the δ-subunits, particularly in the regions that correspond to the P1 and P2 strands of the α-subunits (Noreng et al. 2020) (Figure 3 B); (2) consensus sites for the protease furin, which flank the P1 strand of the GRIP domain, are partly (for human δ-ENaC) or completely (for guinea pig δ-ENaC) absent (Figure 3 C); (3) a key residue that is involved in the coordination of sodium ions and sodium self-inhibition (Asp-338 in human α-ENaC; Noreng et al. 2020) is present in guinea pig α-ENaC (Asp-336), but absent in both human and guinea pig δ-ENaC (Figure 3 C); (4) in comparison with human δ-ENaC, guinea pig δ-ENaC has a slightly longer 'knuckle' region due to the fusion of exons 11 and 12 to a super-exon, adding five amino acids (Figure 3 D). According to the extracellular domain of human α-ENaC (Noreng et al. 2020), the additional

amino acids are likely incorporated into a region that is structurally flexible and located at the protein surface (Figure 3 E and F).

General properties of guinea pig αβγ-ENaC and δβγ-ENaC in comparison to human ENaC isoforms. To investigate the functional properties of guinea pig ENaC isoforms and to compare them to known characteristics of human ENaC orthologues, we heterologously expressed guinea pig or human αβγ- or δβγ-ENaC in *Xenopus laevis* oocytes and recorded whole-cell transmembrane currents (I_M) from oocytes clamped at -60 mV using the two-electrode voltage-clamp technique. ENaC activity was determined as fractions of I_M that were inhibited by 100 µM amiloride, a general ENaC blocker (ΔI_{ami}). Figure 4 A shows representative current traces for oocytes expressing either guinea pig αβγ- or δβγ-ENaCs and demonstrates that both guinea pig ENaC-isoforms are functional ion channels. Water-injected control oocytes did not generate any amiloride-sensitive currents. Guinea pig δβγ-ENaC generated significantly larger ΔI_{ami} (-6.03 ± 0.79 µA, n = 20) than αβγ-ENaC (-2.10 ± 0.21 µA, n = 19, $p < 0.0001$, Student's unpaired t-test with Welch's correction, Figure 4 B). The half-maximal inhibitory concentration (IC_{50}) of amiloride for guinea pig αβγ-ENaC was 0.15 ± 0.02 µM (n = 10), not significantly different from the amiloride IC_{50} for δβγ-ENaC (0.24 ± 0.05 µM, n = 10, p = 0.1095, Mann-Whitney U-test, Figure 4 C). As with the guinea pig ENaCs, human δβγ-ENaC generated significantly larger ΔI_{ami} (-10.23 ± 3.25 µA, n = 10) than human αβγ-ENaC (-6.518 ± 3.192 µA, n = 10, p = 0.0191, Student's unpaired t-test, Figure 4 D/E). The amiloride IC_{50} values for human ENaCs are consistent with published data (Waldmann et al. 1995) in that human δβγ-ENaC (IC_{50} = 2.22 ± 0.26 µM, n = 6) is less sensitive to amiloride than human αβγ-ENaC (IC_{50} = 0.15 ± 0.01 µM, n = 6, p = 0.0022, Mann-Whitney U-test, Figure 4 F). In contrast to αβγ-ENaC, human δβγ-ENaC is more permeable to Na^+ than Li^+ (Waldmann et al. 1995). This trait is not shared by guinea pig δβγ-ENaC which is slightly more permeable to Li^+ over Na^+ (1.07 ± 0.04, n = 19) although not by the same magnitude as guinea pig αβγ-ENaC (1.77 ± 0.11, n = 13, $p < 0.0001$, Mann-Whitney U-test).

The single channel conductance of human δβγ-ENaC is 12 pS (Waldmann et al. 1995; Wesch et al. 2012), which is more than twice as large as αβγ-ENaC (4.9 pS; Fronius et al. 2010). This, together with an increased open probability (Haerteis et al. 2009) explains why the ΔI_{ami} of oocytes expressing human δβγ-ENaC are larger than of those expressing αβγ-ENaC. We determined the single-channel conductance of guinea pig αβγ- and δβγ-ENaC (Figure 4 G/H). The slope conductances (G_{slope}, Figure 4 H) were calculated from linear regressions of recorded unitary conductances at membrane potentials clamped between -100 mV and -20 mV. Interestingly, the G_{slope} of guinea pig αβγ-ENaC (4.43 ± 0.19 pS, n = 10) was not significantly different from the G_{slope} of guinea pig δβγ-ENaC (4.21 ± 0.35 pS, n = 7, p = 0.57, unpaired Student's t-test).

Isoform-specific control of ENaC activity by proteases and sodium. Proteolytic processing of ENaC subunits plays a major role in regulating channel activity. Before αβγ-ENaC reaches the plasma membrane, the α- and γ-ENaC subunits are cleaved in the trans-Golgi network by the endoprotease furin (Kleyman and Eaton 2020). The γ-ENaC subunit is cleaved once while the α-ENaC subunit is cleaved twice, thereby removing an inhibitory peptide within the extracellular domain (Kleyman and Eaton 2020). The release of this inhibitory peptide increases ENaC open probability to a moderate level. When furin-processed ENaC reaches the plasma membrane, the γ-ENaC subunit can be additionally cleaved by extracellular proteases (such as prostasin), thereby releasing the inhibitory peptide from the γ-ENaC subunit and further increasing ENaC open probability (Kleyman and Eaton 2020). A well-established protocol for the assessment of proteolytic ENaC activation in *Xenopus* oocytes is the recording of ΔI_{ami} before and after exposure to the protease chymotrypsin (Haerteis et al. 2009; Wichmann et al. 2018) (Figure 5). Oocytes expressing guinea pig or human ENaCs were perfused with amiloride. Amiloride was removed for 3 min in order to determine baseline ΔI_{ami}. Afterwards, oocytes were perfused for 5 min with chymotrypsin (2 µg/ml) in the presence of amiloride. Drugs and protease were subsequently removed and ΔI_{ami} was determined again (Figure 5 A). The ratio between the two ΔI_{ami} was calculated to reveal fold-changes in ENaC activity due to application of chymotrypsin (Figure 5 B). To account for changes in ENaC activity over time, identical recordings were performed without chymotrypsin as controls. Consistent with published data (Haerteis et al. 2009), both human ENaC isoforms were activated by the application of extracellular protease. The ratio of the two ΔI_{ami} of human αβγ-ENaC expressing oocytes was 0.65 ± 0.04 (n = 8) under control conditions, and significantly increased to 1.77 ± 0.11 (n = 9; $p < 0.0001$, Student's paired t-test) after chymotrypsin exposure (Figure 5 A/B). For oocytes expressing human δβγ-ENaC, the ratio of the two ΔI_{ami} was 0.87 ± 0.03 (n = 8) in protease-free controls and increased significantly to 1.13 ± 0.06 (n = 9, $p = 0.0079$, Student's paired t-test, Figure 5 A/B) in the presence of chymotrypsin. Chymotrypsin thus leads to a much stronger activation of human αβγ-ENaC than human δβγ-ENaC. Similarly, in oocytes expressing guinea pig αβγ-ENaC, the ratio of the two ΔI_{ami} after exposure to chymotrypsin was 1.52 ± 0.08 (n = 13), which was significantly larger than the chymotrypsin-free control (0.76 ± 0.02, n = 12, $p < 0.0001$, Mann-Whitney U-test, Figure 5 C/D). By contrast, oocytes expressing guinea pig δβγ-ENaC did not display any differences in the ratio of the two ΔI_{ami} following the application of chymotrypsin (0.78 ± 0.03, n = 15) or in the chymotrypsin free control group (0.75 ± 0.06, n = 12, $p = 0.9427$, Mann-Whitney U-test, Figure 5 C/D). In summary, whereas αβγ-ENaC is profoundly activated by chymotrypsin, activity of δβγ-ENaC was less affected by protease treatment in both mammalian ENaC orthologues.

In addition to proteolytic processing of ENaC subunits, extra- and intracellular sodium concentrations are important determinants of ENaC activity. ENaC-mediated transmembrane currents typically reduce over time through either feedback inhibition driven by an increase in intracellular sodium concentration or through sodium self-inhibition (SSI) driven by an increase in extracellular sodium concentration (Chraïbi and Horisberger 2002). The magnitude of SSI was calculated as the percentage of the ENaC-mediated current that remained 3 minutes after rapidly switching the sodium concentration in the (extracellular) perfusion solution from 1 mM to 90 mM sodium (Figure 5 E). SSI of guinea pig δβγ-ENaC (16.09 ± 2.49 %, n = 17) was significantly smaller than SSI of guinea pig αβγ-ENaC (46.52 ± 2.708 %, n = 18; $p < 0.0001$, Student's unpaired t-test, Figure 5 F). Under the same experimental conditions, the SSI of the human ENaC isoforms were similar to guinea pig ENaCs in that human δβγ-ENaC showed a significantly smaller SSI (17.72 ± 0.99 %, n = 10) than human αβγ-ENaC (57.68 ± 2.21 %, n = 10, $p < 0.0001$, Mann-Whitney U-test, Figure 5 G/H).

δβγ-ENaC activity is uncoupled from extracellular sodium concentrations. The control of ENaC activity by SSI avoids excessive uptake of sodium ions into the cells under conditions of high extracellular sodium concentrations (Kleyman et al. 2018). Thus, the reduced SSI in guinea pig and human δβγ-ENaC isoforms indicates uncoupling between ENaC activity and the extracellular sodium concentrations ($[Na^+]$). We therefore increased the $[Na^+]$ gradually from 1 mM to 300 mM while the I_M of ENaC expressing oocytes was being recorded. Osmolarity of the extracellular solution was kept constant using N-methyl-D-glucamine as a Na^+ substitute. While the I_M of guinea pig αβγ-ENaC expressing oocytes did not further increase at extracellular $[Na^+]$ beyond 60 mM, there was a continuous increase in I_M of guinea pig δβγ-ENaC expressing oocytes across the employed range of extracellular $[Na^+]$ used (Figure 6 A). Values of I_M at different extracellular $[Na^+]$ were fitted to Michaelis-Menten kinetics (Figure 6 B) to estimate the maximal current generated by each ENaC isoform (V_{max}) and the extracellular $[Na^+]$ at which half the V_{max} is achieved (K_M) (Figure 6 C). Guinea pig δβγ-ENaC has a significantly higher K_M (76.86 ± 4.63 mM Na^+, n = 12) than guinea pig αβγ-ENaC (26.78 ± 4.01 mM Na^+, n = 12, $p < 0.0001$, Mann-Whitney U-test), indicating that the presence of the δ-subunit causes increased ENaC activity at high extracellular $[Na^+]$. The V_{max} of guinea pig δβγ-ENaC was also significantly larger (-7.04 ± 0.68 µA, n = 12) than that of αβγ-ENaC (-3.44 ± 0.79 µA, n = 12, $p = 0.0005$, Mann-Whitney U-test), consistent with the larger ΔI_{ami} recorded in oocytes expressing δβγ-ENaCs as compared to those expressing αβγ-ENaC (Figure 4 A/B).

Similar results were obtained with human ENaC isoforms (Figure 6 D - F). Human δβγ-ENaC also had a significantly higher K_M (73.73 ± 11.33 mM Na^+, n = 10) than αβγ-ENaC (8.71 ± 1.91 mM Na^+, n = 10, $p = 0.0003$, Student's unpaired t-test with Welch's correction). V_{max} of human δβγ-ENaC (-11.88 ± 2.73 µA, n = 10) was larger than αβγ-ENaC (-6.27 ± 1.14 µA, n =

10), but statistical significance was not reached (p = 0.082, Student's unpaired t-test with Welch's correction, Figure 6 F). Nevertheless, the presence of the δ-subunit appears to increase ENaC activity at high extracellular [Na^+] in both human and guinea pig ENaCs.

Reduced sodium self-inhibition is pivotal to ENaC activity at high extracellular sodium concentrations. Proteolytic processing of ENaC subunits and SSI are linked regulatory processes. Cleavage of human αβγ-ENaC expressed in *Xenopus* oocytes causes a reduction in the magnitude of SSI (Chraïbi and Horisberger 2002) whereas mutations in furin cleavage sites that prevent proteolytic processing in mouse α-ENaC causes increased SSI (Sheng et al. 2006). We recorded SSI of guinea pig αβγ-ENaC with and without prior incubation in chymotrypsin (2 µg/ml in NMDG-ORS) for 5 minutes (Figure 7 A). After incubation in chymotrypsin, SSI of guinea pig αβγ-ENaC was 19.28 ± 1.57 % (n = 15), significantly smaller than the SSI of guinea pig αβγ-ENaCs that were not treated with chymotrypsin (59.83 ± 3.19 %, n = 8, p < 0.0001, unpaired Student's t-test, Figure 7 B). The I_M of guinea pig αβγ-ENaCs with and without prior incubation with chymotrypsin were then recorded as the extracellular [Na^+] was increased from 1 mM to 300 mM (Figure 7 C). Exposure of guinea pig αβγ-ENaC to chymotrypsin significantly increased V_{max} (-11.93 ± 1.69 µA) and K_M (44.87 ± 4.06 mM Na^+, n = 15) as compared to untreated αβγ-ENaCs (V_{max}: -4.65 ± 0.37 µA, n = 11, p = 0.0009, unpaired Student's t-test with Welch's correction; K_M: 17.56 ± 6.03 mM Na+, p < 0.0001, Mann-Whitney U-test, Figure 7 E/F). These data indicate that proteolytic reduction of SSI in guinea pig αβγ-ENaC enhances ENaC activity across the range of extracellular [Na^+] used and resembles the activity of guinea pig δβγ-ENaC (Figure 6) which has an inherently reduced SSI and lacks proteolytic activation (Figure 5).

The reduced sodium self-inhibition of human and guinea pig δβγ-ENaC generates increased activity at high extracellular sodium concentrations. We observed that both human and guinea pig δβγ-ENaC are more active at high extracellular [Na^+] than αβγ-ENaCs (Figure 6). Human and guinea pig δβγ-ENaC have a reduced SSI (Figure 5) and the I_M - [Na^+] relationship is altered by a change in the magnitude of SSI (Figure 7). We therefore hypothesised that the magnitude of SSI of guinea pig and human δβγ-ENaC is reduced across the employed range of extracellular [Na^+], thereby establishing increased ENaC activity. We recorded SSI of guinea pig αβγ- and δβγ-ENaC expressing oocytes at extracellular [Na^+] between 3 mM and 300 mM (Figure 8 A). The magnitude of SSI in guinea pig αβγ-ENaC (Figure 8 B) increased steadily from 35.69 ± 3.98 % at 3 mM extracellular [Na^+] to 73.15 ± 1.25 % at 300 mM extracellular [Na^+], while the magnitude of SSI of guinea pig δβγ-ENaC appeared to decline slightly as extracellular [Na^+] increased. The relationship between SSI and the extracellular [Na^+] was described by the slope derived from linear regression of SSI at logarithmic transformations of extracellular [Na^+] between 3 mM and 300 mM (Figure 8 B). The

slope of the regression line of guinea pig αβγ-ENaC (21.02 ± 2.37, n = 6-9) was significantly larger than that of δβγ-ENaC (-6.20 ± 1.81, n = 6-10, ANCOVA, $p < 0.0001$, $F_{1, 135} = 84.01$). A similar result was obtained when the magnitudes of SSI of human ENaCs orthologues were estimated using the same protocol (Figure 8 C). The slope of the linear regression of human αβγ-ENaC (15.72 ± 3.44, n = 9) was also significantly larger than that of δβγ-ENaC (3.37 ± 3.73, n = 9-11, ANCOVA, $p = 0.0166$, $F_{1, 142} = 5.879$, Figure 8 C). In sum, these data indicate that the reduced SSI uncouples the control of δβγ-ENaC activity from extracellular [Na^+], thereby leading to enhanced ENaC-mediated sodium uptake across a wide range of extracellular sodium concentrations.

Functional gene coding for δ-ENaC is not associated with habitat aridity across Rodentia. In mammals, ENaC plays an important role in fine-tuning renal sodium re-absorption and extracellular fluid volume as part of the RAAS (Schild 2010). It is therefore considered a key player in the control of sodium and water homeostasis. Interestingly, mammals living in dry (arid) habitats appear to have higher basal levels of the RAAS (Donald and Pannabecker 2015), and recent studies indicated that enhanced ENaC activity drives renal water re-absorption and faecal dehydration in desert mammals (Wu et al. 2014; Zhang et al. 2019). Since δβγ-ENaCs have an enhanced activity as compared to αβγ-ENaCs and would therefore enhance sodium and, consequently, water conservation, we explored whether the presence of the δ-subunit in a rodent species might correlate with associated environmental factors. Geolocation data extracted from the Global Biodiversity Information Facility (GBIF) were used to plot the global distribution of non-invasive rodent species that maintained a functional *SCNN1D* and those that lost it (Figure 9, Supplemental Figures 2 - 5). Invasive rodent species, as described in the Global Invasive Species database, were excluded from the analysis in order to focus on the natural species' distributions (Supplemental Figure 5). In Sciuromorpha, loss of *SCNN1D* was observed in North American, East Asian and South African species (Figure 9). Interestingly, most of the species lacking *SCNN1D* are adapted to cold and warm arid environments (Supplemental Figure 2) (Wilson et al. 2017). In Supramyomorpha, species lacking *SCNN1D* are widely distributed across various climates in North America, Africa and South-East Asia (Figure 9, Supplemental Figure 3). Interestingly, all Hystricomorpha species we investigated maintained functional *SCNN1D* independent of habitat aridity, except for the Patagonian mara (*D. patagonum*) (Figure 9, Supplemental Figure 4). Based on a potential habitat-dependent distribution of rodents with and without functional *SCNN1D* among Sciuromorpha, we tested whether its presence partially explained variation in habitat aridity. Species with and without the gene (n = 43) were found distributed across a wide range of habitat aridities (Figure 9). However, inclusion of gene presence did not significantly improve model fit compared to the null model of random species effects only ($\chi^2_{(1)}$

= 1.20, p = 0.273), with random species effects alone explaining 49.5 % of the observed variance in aridity (*cf*. 52.2% conditional r^2 for the model with gene presence). Modelling more complex phylogeny (species nested within clade) could not be resolved due to singular fits of the mixed effects models. Therefore, evidence based on this statistical analysis suggests that the presence of a functional *SCNN1D* does not appear to be associated with observed aridity across Rodentia given species level differences in habitat.

Discussion

This study closes an intriguing gap in knowledge regarding functional δ-ENaC in rodents, which has puzzled the field of ENaC research for more than twenty years - to the point that rodents had been assumed to lack a functional *SCNN1D* gene (Kleyman and Eaton 2020; Paudel et al. 2021). Based on an investigation of likely functional δ-ENaC-encoding *SCNN1D* genes in rodent genomes, we report that *SCNN1D* is not generally absent from rodents but was independently lost in at least five rodent clades, including the Muridae family (rats and mice). We note that previous studies employing RT-PCR indicated the presence of *SCNN1D* in mouse (Nie et al. 2009), but the entire gene has never been fully identified and its gene product has never been cloned. Given the current sequence coverage of the mouse genome, its position would have been identified. Hence, previously reported RT-PCR data (Nie et al. 2009) are likely due to residual *SCNN1D* promoter activity that does not result in a functional mRNA.

The 'loss of the *SCNN1D*' gene was actually a loss of function due to frame-shifts, preliminary stop signals or disruptions of splice-donor and splice-acceptor sites, rather than complex genomic rearrangements resulting in a deletion of genomic information, leaving its flanking genes, *UBE2J2* and *ACAP3*, intact. Further, changes to a likely functional *SCNN1D* gene arose in the infraorder Hystricognathi, resulting in a fused super-exon consisting of exons 11 and 12 with the separating intron. Exons 11 and 12 code for the ENaC 'knuckle' domain which interacts with the finger domains of the neighbouring ENaC subunits (Noreng et al. 2018) and plays an important role in sodium self-inhibition (SSI) (Chen et al. 2015). Strikingly, the incorporation of additional amino acids into this region of guinea pig δ-ENaC due to the exon fusion does not affect channel functionality. This is likely due to the peripheral location of the knuckle domain at the channel surface, which allows substantial flexibility in contrast to other domains which are, e.g., involved in key parts of the gating machinery of the ion channel.

The most parsimonious explanation is that the 'super-exon' is a new autapomorphic feature of Hystricognathi. This clade comprises Hystricidae (Old World porcupines), Phiomorpha (African cane rats, dassie and mole rats) and Caviomorpha (New World hystricognaths. i.e., cavies and allies) (Patterson and Upham 2014). The oldest known

Hystricognathi are the caviomorphs *Canaanimys maguiensis*, *Cachiyacuy kummeli* and *Cachiyacuy contamanensis* from the late Middle Eocene (~41 Ma) of Peru (Antoine et al. 2012). However, the origin of Hystricognathi is certainly in Asia and dates back into the Early Eocene or even Late Palaeocene (up to 56 Ma), although the oldest phiomorph fossils are known from younger deposits in the Middle Eocene of North Africa (Antoine et al. 2012; Marivaux et al. 2014; Patterson and Upham 2014). The oldest Hystricidae are members of the genus *Atherurus* which were found in Late and Middle Miocene deposits of Pakistan (~15 Ma) and Egypt (~11 Ma) (Weers 2005; Mein and Pickford 2006). Thus, we can confidently conclude that the fusion of exons 11 and 12 evolved in the Eocene at the latest because it was already present in the last common ancestor of Hystricognathi. Although the super-exon may not very substantially affect the function of δβγ-ENaC in general, it has been a stable feature for more than 41 Ma.

Functional analyses of guinea pig αβγ- and δβγ-ENaCs expressed in *Xenopus* oocytes allowed us to compare their biophysical and regulatory properties with human ENaC orthologues. Compared to αβγ-ENaCs, we found that guinea pig δβγ-ENaCs, (1) generate larger transmembrane currents; (2) have a reduced sensitivity to extracellular proteases; (3) have a reduced SSI; and (4) exhibit uncoupling between the control of channel activity and the extracellular [Na^+]. These characteristics are similar to those of the human ENaC orthologues. As a constitutively active ion channel, the transmembrane current generated by ENaC activity depends on the number of active channels in the plasma membrane, the single channel conductance and the open probability. Previous studies showed that δ-subunit incorporation does not lead to an increased membrane abundance of human (Haerteis et al. 2009) and *Xenopus laevis* δβγ-ENaCs (Wichmann et al. 2018). Assuming, accordingly, that there is also no difference in the membrane abundance between guinea pig δβγ-ENaC and αβγ-ENaC, the observed differences in transmembrane currents and in coupling between ENaC current and the extracellular [Na^+], are likely caused by different single channel conductance or open probability.

The single channel sodium conductance of human δβγ-ENaC is more than twice as large as that of αβγ-ENaC (Waldmann et al. 1995; Wesch et al. 2012). This seems to be a novel feature of human ENaCs, as the single channel sodium conductances of guinea pig and *Xenopus laevis* αβγ- and δβγ-ENaCs are similar (Wichmann et al. 2018). Unlike the human isoforms, the difference in transmembrane currents between guinea pig ENaC isoforms is not related to a larger single channel conductance of δβγ-ENaC, so that the difference between transmembrane currents of guinea pig αβγ- and δβγ-ENaCs and the relationship between transmembrane currents and extracellular [Na^+], are likely due to differential ENaC open probabilities. Indeed, proteolytic processing and sodium self-inhibition, key control

mechanisms of ENaC open probability (Kleyman and Eaton 2020), are reduced in guinea pig and human δβγ-ENaCs.

The Cryo-EM-derived structure of human αβγ-ENaC reveals a domain that is unique to ENaC and referred to as the Gating Relief of Inhibition by Proteolysis (GRIP) domain (Noreng et al. 2018). The peptide sequence that forms the GRIP domain resides between the α1 and α2 helices of the 'finger' domain and contains inhibitory tracts that are released when ENaC is cleaved by proteases. The intracellular protease furin cleaves ENaC within the Golgi apparatus at the consensus site (Arg-X-X-Arg) (Molloy et al. 1992). The human α-ENaC subunit has two furin consensus sites within the GRIP domain and is cleaved twice by furin. This removes the inhibitory peptide and changes ENaC from a near silent channel to one with an intermediate open probability (Kleyman and Eaton 2020). The γ-ENaC subunit is only cleaved once by furin. The activation of membrane bound ENaC is attributed to a second cleavage of γ-ENaC by extracellular proteases, releasing the inhibitory tract from γ-ENaC. This switches ENaC to a high open probability, increasing its activity (Kleyman and Eaton 2020). Consistent with previous reports (Haerteis et al. 2009), human αβγ- and δβγ-ENaCs are activated by extracellular proteases, but the activity increase of human δβγ-ENaC is smaller than that of αβγ-ENaC. While the activity of guinea pig αβγ-ENaC is increased, the activity of δβγ-ENaC did not change upon application of extracellular protease. Guinea pig δ-ENaCs lack the two furin consensus sites that are present in the α-subunit (Wichmann et al. 2019; Wichmann and Althaus 2020). Further, we showed previously that the presence of the δ-subunit in *Xenopus laevis* δβγ-ENaCs prevents extracellular protease (chymotrypsin) from cleaving the γ-subunit (Wichmann et al. 2019). It is thus likely that the insensitivity of guinea pig δβγ-ENaC to extracellular protease is caused by the absence of furin cleavage sites in δ-ENaC and prevention of γ-subunit cleavage. We also observed that the peptide sequences of human and guinea pig δ-ENaC GRIP domains are shorter than those of α-ENaC in both species, particularly in the region encompassing the P1 and P2 strands of the α-subunits GRIP domains. Removal of the P1 strand was recently suggested to cause the loss of SSI after proteolytic cleavage (Noreng et al. 2020). Thus, the shorter GRIP domains of human and guinea pig δ-ENaC may explain the greatly reduced SSI in human and guinea pig δβγ-ENaCs.

Previous studies demonstrated that proteolytic processing activates ENaC by relieving SSI (Chraïbi and Horisberger 2002). As shown in this and previous studies (Ji et al. 2006), the magnitude of SSI is lower in human δβγ-ENaCs than in human αβγ-ENaCs. In line with the human ENaC isoforms, the magnitude of SSI in guinea pig δβγ-ENaCs is also reduced as compared αβγ-ENaCs. SSI likely involves the coordination of sodium ions in an extracellular region termed the acidic cleft (Kashlan et al. 2015; Wichmann et al. 2019). A key residue that likely coordinates sodium ions was identified the β6-β7 loop of the acidic cleft of human and mouse α-ENaC (Asp-338 and Asp-365, respectively) (Kashlan et al. 2015; Noreng et al. 2020)

and of *Xenopus laevis* δ-ENaC (Asp-296), which, in contrast to mammalian δβγ-ENaCs, shows a strong SSI. This conserved residue is absent from human and guinea pig δ-ENaCs (Wichmann et al. 2019), which might further contribute to the reduced SSI in these variants. In addition to the residues in the acidic cleft, intra-subunit interactions between the 'finger' and 'knuckle' domains of neighbouring ENaC subunits are likely required to translate sodium binding in the acidic cleft to a change in the channel gate (Wichmann et al. 2019). This supports the idea that the shorter GRIP domains of human and guinea pig δ-ENaC may contribute to a reduced SSI by restricting conformational changes in the channels. Further, deletion of the 'knuckle' domain in the α-subunit of mouse ENaC results in loss of SSI (Chen et al. 2015). The altered structure of the 'knuckle' domain due to exon fusion in guinea pig δ-ENaC might therefore also contribute to structural impairments that reduce SSI.

Consistent with previous reports on human ENaC (Chraïbi and Horisberger 2002), the magnitude of SSI increases with the extracellular [Na^+] in human and guinea pig αβγ-ENaCs, a phenomenon that was suggested to protect epithelial cells from absorbing excess sodium ions (Kleyman et al. 2018). SSI is a dynamic mechanism for regulating ion channel activity that responds instantaneously to changes in urinary [Na^+]. This coupling of ENaC activity to the extracellular [Na^+] is absent from human and guinea pig δβγ-ENaCs, resulting in increased ion channel activity as the extracellular [Na^+] rose above approximately 60 mM. This enhanced activity under high extracellular [Na^+] is linked to the reduced SSI in these ENaC isoforms. Previous studies on mouse αβγ-ENaC showed that the magnitude of SSI is reduced in proteolytically processed channels (Sheng et al. 2006). In addition, prevention of proteolytic processing of mouse α-ENaC by mutating the furin consensus sites increases the magnitude of SSI (Sheng et al. 2006). Consistently, exposure of guinea pig αβγ-ENaC to chymotrypsin led to SSI reduction and increased ion channel activity at higher extracellular [Na^+]. Interestingly the K_M and V_{max} of the cleaved αβγ-ENaC were more than twice as big as those of uncleaved αβγ-ENaC, mirroring the difference between the K_M and V_{max} of the human and guinea pig δβγ- and αβγ-ENaC isoforms. In this instance the proteolytically processed αβγ-ENaC behaves like the protease-insensitive δβγ-ENaC and displays greater activity at higher extracellular [Na^+].

In summary, guinea pig and human δβγ-ENaCs have an increased activity as compared to αβγ-ENaCs, and channel activity is not curbed at high extracellular [Na^+] due to a strongly reduced SSI. Assuming that these characteristics are conserved among rodent ENaCs, the question of a physiological context in which such properties might be advantageous arises. Key targets for the RAAS are the distal convoluted tubules and cortical collecting ducts in the mammalian kidney, where aldosterone controls αβγ-ENaC expression to match sodium excretion to dietary sodium intake (Palmer and Schnermann 2015). The RAAS evolved in tetrapod vertebrates as an adaptation to a terrestrial environment, and, to

the best of our knowledge, there is no tetrapod vertebrate species that lacks genes coding for αβγ-ENaC. Given the physiological importance of αβγ-ENaC, we searched for evidence indicating that δβγ-ENaCs displaying increased activity (as compared to αβγ-ENaC) might be an advantage for rodent species living in particularly arid environments with higher physiological demands on sodium and water homeostasis.

The loss of *SCNN1D* represents an apomorphic feature that evolved independently in all three major rodent clades. In the Sciuromorpha this trait is restricted to the Sciuridae, which at first glance indicates a phylogenetic signal. However, our sciurid sample comprises only ground squirrels of the subfamily Xerinae, more specifically, of the tribes Xerini and Marmotini (Steppan et al. 2004). Thus, representatives of the third xerine tribe Protoxerini and further species of the other sciurid subfamilies need to be investigated in order to test a phylogenetic signal for the respective taxon level. Although our results clearly show that loss of *SCNN1D* cannot generally be related to aridity of the habitat of the investigated species across Rodentia, there appears to be a climate-related signal within the Sciuridae under study. All the investigated Xerini are adapted to cold and warm arid environments like mountain regions, steppes, prairie, and (semi)deserts (Wilson et al. 2017). One exception is *Marmota monax* which is widely distributed from Alaska and Canada into open lowland environments of the eastern United States, covering a wide range of ecosystems and climates (Wilson et al. 2017) (Supplemental Figure 2). According to Polly (2003), *Marmota monax* subspecies evolved and differentiated over several glacial cycles within the last 750,000 years whereas other extant North American *Marmota* species evolved more recently. The observed higher diversity of molar shape in *Marmota monax* may reflect their greater adaptive potential due to repeated geographic fragmentation and thus could explain the wide range in habitat climates observed today. Another exception is *Marmota marmota*, whose environment has the highest mean humidity among the studied sciurid species we studied, although most of the observation sites refer to arid environments (see Figure 9 and Supplemental Figure 2). In the Alps, this species prefers habitats that match less vegetation and high sun exposure with early snowmelt (Allaine et al. 1994). However, future investigations of tree squirrels (Protoxerini, Sciurinae and other subfamilies) need to prove the *SCNN1D* loss as a potential ecological adaptation in Sciuridae.

Among Supramyomorpha the loss of *SCNN1D* is restricted to Heteromyidae, Dipodidae and certain Muroidea. Besides being a potential phylogenetic signal (autapomorphic), the *SCNN1D* loss in Heteromyidae and Dipodidae could be also constrained by the arid environment the investigated species live in (Wilson et al. 2016; Wilson et al. 2017). Concerning Muroidea, the *SCNN1D* loss may be a synapomorphic character of Eumuroida, a clade comprising Nesomyidae, Cricetidae and Muridae. Future studies of Calomyscidae need to prove if the *SCNN1D* loss is characteristic of a more exclusive clade. However, no climatic or dietary signals are evident as our sample comprises species with very diverse diets

(omnivorous, herbivorous, insectivorous), habitats and geographic distributions (Wilson et al., 2017). This indicates that the loss of *SCNN1D* is not a disadvantage for the respective species.

Within Hystricomorpha only *Dolichotis patagonum* lost *SCNN1D*, although many members of this suborder inhabit arid environments. The Patagonian mara differs from other caviomorph rodents in reflecting a small ruminant adapted to open grass grasslands. However, a study on the digestive system and metabolic rates of *Dolichotis patagonum* shows no significant differences from other caviomorphs (Clauss et al. 2019). Therefore, no plausible explanation for the derived pattern in *Dolichotis patagonum* can be provided at this point.

In general, possible geographic patterns (e.g., presence of *SCNN1D* in South American species, absence of *SCNN1D* in East Asian species) are certainly biased by our taxon sampling. For instance, given the fact that the Cricetidae members we investigated are all showing *SCNN1D loss,* it is likely that South American members of this family, which were not included in our study, also show the same pattern. Further, the available GBIF data might be biased as numbers of individual observations vary substantially between species. Nevertheless, the broad geographical distribution of species lacking *SCNN1D* - including the Eumuroida - indicates that the absence of *SCNN1D* does not appear to be a general disadvantage or adaptation to an extreme environmental climate. Rather, our data indicate that the role of δβγ-ENaC in renal sodium and water homeostasis might not be as crucial as that of αβγ-ENaC.

Whether δ-ENaC is regulated by aldosterone, expressed in the mammalian distal nephron, or forms functional δβγ-ENaCs in the kidney remains unknown. None of the analysed rodent species with a functional *SCNN1D* appears to lack a *SCNN1A* gene coding for α-ENaC (data not shown). Given the efficacy of the RAAS in controlling sodium and water homeostasis across a wide range of mammalian species living in various environments, there does not appear to be any obvious benefit in an additional ENaC isoform with high activity in renal tubules. Further, $[Na^+]$ in the distal convoluted tubules and cortical collecting ducts are lower than plasma $[Na^+]$ and, based on the I_M - $[Na^+]$ relationships observed in this study, differences in the activity between αβγ-ENaCs and δβγ-ENaC appear unlikely under these conditions. This might explain why pseudogenisation of *SCNN1D* does not appear to correlate with habitat aridity across Rodentia.

The specific I_M - $[Na^+]$ relationships might indicate that δβγ-ENaC operates under extracellular $[Na^+]$ that are equal or greater than plasma $[Na^+]$. In humans, RNA and protein expression of δ-ENaC was observed in taste buds, which are exposed to a wide range of dietary $[Na^+]$, including concentrations that greatly exceed plasma $[Na^+]$ (Bigiani 2020a). In mice, αβγ-ENaC is involved in attractive salt taste to $[Na^+]$ lower than plasma $[Na^+]$ (Chandrashekar et al. 2010; Nomura et al. 2020). In humans, the role of ENaC in salt taste is unclear (Bigiani 2020b) but it was recently suggested that δ-ENaC might be relevant for the

detection of [Na^+] that exceed plasma [Na^+] (Bigiani 2020b). The functional properties of δβγ-ENaC we observed here would be consistent with this notion. δβγ-ENaC could be involved in mechanisms triggering aversive responses to potentially dangerous [Na^+] that exceed plasma [Na^+] and renal urine concentration capacity. Such a secondary role in 'danger signalling' might explain the lack of obvious selection pressures maintaining *SCNN1D* purely based on environmental factors. Of note, current understanding of salt taste in rodents is based on studies using mice (Chandrashekar et al. 2010; Nomura et al. 2020) which lack functional δ-ENaC and may have evolved alternative mechanisms for aversive salt taste signalling.

Taken together, the data presented here show that *SCNN1D* is not generally absent across rodents and that pseudogenisation appeared independently in different clades. Despite genomic changes such as exon fusions, guinea pig δβγ-ENaC is a functional ion channel which has biophysical and regulatory characteristics that are very similar to those of the human orthologue. Guinea pigs are therefore suitable, commercially available rodent model animals that allow future investigations to shed light on the physiological function of δβγ-ENaC.

Materials and Methods

Bioinformatical analyses: Bioinformatical and phylogenetic analyses investigating the absence or presence of *SCNN1D* genes were performed essentially as has been described previously (Maxeiner et al. 2020). In short, the search query '*SCNN1D* and rodentia' yielded results for some but not all currently annotated rodent genomes. Those in which *SCNN1D* was present were consistently flanked by the neighbouring genes *UBE2J2* and *ACAP3*. In cases in which *SCNN1D* was not annotated, we used this particular genomic region and performed a sequence alignment to identify potential traces of a not yet annotated or by mutation decaying *SCNN1D* (pseudo-) gene. Information from the latter case were included in a phylogenetic tree based on the otherwise highly conserved exon 6 present and retained in size throughout all *SCNN1* genes (cf. Supplemental Figure 1). Additionally, in our evolutionary assessment based on the phylogeny of rodent families reported by D'Elia et al. (2019) we extended our search employing the BLAST tool to search within distinct rodent families with default settings for blast and megablast searches. Supplemental Data Sheet 1 compiles the information that we retrieved from our search regarding exons sizes etc.

The following sources were used for this study: NCBI databases (https://www.ncbi.nlm.nih.gov/gene/), BLAST tool (https://blast.ncbi.nlm.nih.gov/Blast.cgi), Expasy sequence translation (https://web.expasy.org/translate/), multiple sequence alignment tools MultAlin (Corpet 1988; http://multalin.toulouse.inra.fr/multalin) and Clustal Omega (https://www.ebi.ac.uk/Tools/msa/clustalo/), DNA/RNA GC Content Calculator (http://www.endmemo.com/bio/gc.php), graphical codon usage analyser (codon usage,

https://gcua.schoedl.de), DNA reverse complement tool (http://reverse-complement.com), and phylogeny tool MEGA X (Kumar et al. 2018).

Images of ENaC structures were based on the cryo-EM-derived structures of human αβγ-ENaC (PDB code 6BQN) (Noreng et al. 2018) and the extracellular domain of human αβγ-ENaC (PDB code 6WTH) (Noreng et al. 2020). Structures were visualised with open-source PyMol (Version 2.0, Schrödinger, LLC).

To investigate the geographical distribution of rodent species and correlate functional *SCNN1D* with habitat aridity, positive occurrence data for Rodentia were downloaded from the Global Biodiversity Information Facility (GBIF 2020). GBIF is an international network and data infrastructure that provides open access to over 60,000 species-location datasets, from historical museum specimens and collections through to georeferenced smartphone photographs, that are combined using common data standards into a singular database of almost 2 billion occurrence records that can be queried. We extracted all positive occurrence data for Rodentia, excluding those from zoological institutions (accessed 24th September 2020, for the specific download information, see GBIF 2020). This initial dataset was restricted to georeferenced observations (i.e., those with a known latitude and longitude). We further excluded occurrence data observed prior to 1900 due to the potential increase in misidentification. We limited the dataset to the 51 species for which genomes descriptions are available (cross-referencing potential differences in taxonomic naming, see table 1 for discrepancies). Species were cross referenced against the Global Invasive Species Database (GISD, available at http://www.iucngisd.org/gisd/), which is managed by the Invasive Species Specialist group of the IUCN, with 8 species deemed to be invasive (see Table 1). These were excluded due to their likely occurrence beyond their natural distribution within the GBIF database, biasing further analyses. The resulting dataset consisted of 223,392 geolocated observations for 43 species. To check the quality of the dataset, occurrence locations were mapped for each species and cross-checked against their natural distributions according to (Wilson et al. 2016; Wilson et al. 2017). Records falling outside of known species' ranges were removed along with observations that mapped onto the marine environment, resulting in a cleaned dataset of 218,410 observations (Supplemental Figures 2 - 5). Global aridity data was accessed from the Global Aridity Index and Potential Evapotranspiration Climate Database v2, which is supported by the CGIAR Consortium for Spatial Information (accessed 24th September 2020, available at https://doi.org/10.6084/m9.figshare.7504448.v3). The aridity index estimated as the ratio of mean annual precipitation to mean annual reference evapo-transpiration, and is provided as a 30 arc-second resolution (approximately 30m) raster giving the 30-year average for the period 1970-2000 modelled using the WorldClim Global Climate Data (for details on methodology, see Trabucco and Zomer (2018) and https://cgiarcsi.community/2019/01/24/global-aridity-index-and-potential-evapotranspiration-

climate-database-v2/). For each rodent observation, we extracted an aridity index taken as the median of all aridity surface values encompassed within radius of 0.02º of the observation (approximately 2 km), to limit potential anomalies in microclimates.

Nucleic acid isolation: Guinea pigs (*Cavia porcellus*; "Hartley GP, retired breeders") were purchased from Charles River Laboratories (Sulzfeld, Germany). All animal handling was approved of and followed the standards set by the animal welfare and ethics committee of Saarland University and the local authorities. Tissue samples for nucleic acid extraction were collected in TRIzol® reagent for RNA extraction (Invitrogen, Carlsbad, CA, USA) and DNA extraction was performed from blood samples using the Quick-DNA MiniPrep Plus extraction kit (Zymo Research Europe GmbH, Freiburg, Germany) according to the manufacturer's protocol. RNA extraction strategies involved traditional TRIzol/chloroform extraction with 2-propanol precipitation or purification by column resin using the Direct-zol RNA MiniPrep Plus kit (Zymo Research Europe GmbH). Nucleic acids were quantified using a NanoDrop One spectrophotometer (VWR International GmbH, Darmstadt, Germany) and stored until further use at -80 °C.

5'RACE experiment: In order to determine the transcriptional start of all four guinea pig *SCNN1* genes, cDNA was generated from testis and brain RNA using the SMARTer® RACE 5'/3' Kit (Takara Bio USA, Inc., Mountain View, CA, USA) and followed the manufacturer's protocol generating amplicons using a nested primer approach. All gene specific oligomers were purchased from IDT (Coralville, IO, USA). The 5'RACE cloning strategy aimed at the inclusion of at least a single exon/exon junction to rule out artifacts of potential transcriptional start sites from contaminations of genomic DNA. All amplicons were cloned into a pRACE mini vector using the In-Fusion HD Cloning Kit (Takara Bio USA, Inc.; Mountain View, CA, USA) and validated by Sanger sequencing (ATGC-Lab, MPI for Experimental Medicine, Göttingen, Germany).

Cloning of guinea pig SCNN1 genes: Based on current sequence information (NCBI), primers were designed for PCR amplification aiming at a full coverage of the potential guinea pig *SCNN1D* gene. Due to the relatively high GC content of the genomic region, a combination of polymerases has been applied to yield in a full coverage of the gene, such as PrimeSTAR® HS DNA Polymerase, SeqAmp DNA Polymerase (both: Takara Bio USA, Inc.), or Q5 High-Fidelity 2X Master Mix (New England Biolabs GmbH, Frankfurt, Germany). The products were subcloned by Gibson assembly strategies using the NEBuilder® HiFi DNA Assembly Cloning Kit (New England Biolabs GmbH). Based on bioinformatical analyses of the *SCNN1A*, *B* and *G* genes as well as our own results of the *SCNN1D* gene sequencing effort, the coding

sequence was inferred and mini genes custom-synthesized (gblocks from IDT, Leuven, Belgium) with an optimized codon usage applying to the *Xenopus* expression system. Subsequently, all mini genes were cloned into an *Eco*RI/*Xba*I linearized pTNT™ vector (Promega Corporation, Madison, WI, USA).

Sequence deposition: The sequence information of all guinea pig *SCNN1* 5'RACE sequences (*SCNN1A*, *SCNN1B*, *SCNN1G* and *SCNN1D*) as well as the full coverage of the guinea pig *SCNN1D* gene were deposited with NCBI GenBank using the following accession numbers: *SCNN1A* 5'RACE product (MN187466); *SCNN1B* 5'RACE product (MN187463); *SCNN1G* 5'RACE product A (MN187464); *SCNN1G* 5'RACE product B (MN187465); *SCNN1D* 5'RACE short version (MN187468); *SCNN1D* 5'RACE long version (MN187469); *SCNN1D* gene (MN187539).

Plasmids and cRNA synthesis: The DNA coding sequences for guinea pig, human, and *Xenopus laevis* α, β, γ and δ-ENaC subunits were cloned into the pTNT expression vector (Promega Corporation). Plasmids were transformed into *Escherichia coli* (K12, DH5α) and isolated using QIAprep Spin Miniprep kit (Qiagen, Manchester, UK). Plasmid cDNAs for human ENaC subunits were linearized with FastDigest *Bam*HI (ThermoFisher Scientific, Gloucester, UK) per manufacturer's instructions. The guinea pig ENaC subunits were not linearized due to presence of restriction sites within the coding sequences. ENaC subunit cRNAs were generated by *in vitro* transcription with T7 RNA polymerase (Ribo-MAX large-scale RNA production system, Promega Corporation) in accordance with the manufacturer's instructions. The ENaC subunit cRNAs were then diluted with diethyl pyrocarbonate (DEPC)-treated water to a final concentration of 10 ng/µl for human and 5 ng/µl for guinea pig ENaCs for two-electrode voltage-clamp recordings. For patch-clamp recordings, guinea pig ENaC cRNA was diluted to 20 ng/µl per subunit.

Isolation of* Xenopus *oocytes and cRNA injection: The experimental procedures were approved by the Animal Welfare and Ethical Review Body at Newcastle University (project ID 630). *Xenopus laevis* ovaries were purchased from the European *Xenopus* Resource Centre (EXRC, Portsmouth, UK). Ovary lobes were manually dissected with forceps before being incubated and rocked (40 rpm) for 90 minutes in Oocyte Ringer Solution II (ORII; 82.5 mM NaCl, 2 mM KCl, 1 mM $MgCl_2$, 5 mM HEPES, pH 7.5) containing 2.6 mg/ml collagenase A (Roche, Welwyn Garden City, UK) in order to remove the follicular cell layer. Oocytes were then washed 6 times with ORII and washed a further 6 times with Modified Barth's Solution (MBS; 88 mM NaCl, 1 mM KCl, 0.41 mM $CaCl_2$, 10 mM HEPES, 2.4 mM $NaHCO_3$, 0.33 mM $Ca(NO_3)_2$, 0.82 mM $MgSO_4$, 20 µg/ml gentamycin, pH 7.5). Stage V and VI oocytes were

manually selected and placed in MBS. Oocytes were injected (Nanoject automatic oocyte injector, Drummond Scientific, Broomall, PA, USA) with 13.8 nl of αβγ- or δβγ-ENaC cRNA and incubated at 16 °C for 16-24 hours in low sodium N-Methyl-D-Glucamine-Oocyte Ringer Solution (NMDG-ORS; 80 mM NMDG, 10 mM NaCl, 1 mM KCl, 2 mM $CaCl_2$, 2.5 mM Sodium pyruvate, 5 mM HEPES, 20 μg/ml gentamycin, pH 7.4). For patch-clamp recordings, oocytes were incubated for 2-7 days.

Two-electrode voltage-clamp recordings: Oocytes were clamped at a holding potential of -60 mV using a Warner oocyte voltage clamp amplifier (OC725B/C Warner Instruments, Hamden, CT, USA). Whole cell transmembrane current signals (I_M) were filtered at 1 kHz and were recorded using a strip chart recorder. Oocytes were superfused at room temperature with Oocyte Ringer Solution (ORS; 90 mM NaCl, 1 mM KCl, 2 mM $CaCl_2$, 5 mM HEPES, pH 7.4) at a perfusion speed of 3-5 ml/min, unless otherwise stated. The application of amiloride (Alfa Aesar, Heysham, UK) was used to determine the fraction of the I_M that was generated by ENaC (amiloride-sensitive current, ΔI_{ami}).

Patch-clamp recordings: Patch-clamp recordings were performed using the cell-attached configuration as previously described (Wichmann et al. 2019). Mechanically devitellinized oocytes were placed in a recording chamber filled with bath solution (145 mM KCl, 1.8 mM $CaCl_2$, 10 mM HEPES, 2 mM $MgCl_2$, 5.5 mM glucose, pH 7.4). Borosilicate glass capillaries were used to generate patch-pipettes (6-10 MΩ resistance) by employing a two-stage puller (PP83, Narishige, London, UK). The patch-pipettes were then heat polished before being filled with pipette solution (145 mM NaCl, 1.8 mM $CaCl_2$, 10 mM HEPES, 2 mM $MgCl_2$, 5.5 mM glucose, pH 7.4). A LM-PC patch-clamp amplifier (List-Medical, Darmstadt, Germany) was used to amplify current signals which were low-pass filtered at 100 Hz (Frequency Devices, Haverhill, IL, USA). Current signals were recorded at 2 kHz using an Axon 1200 interface with Axon Clampex software (Axon Instruments, Foster City, CA, USA). All experiments were performed at room temperature. Single channel analysis was performed using Clampfit 10.7 software (Molecular Devices, Wokingham, UK).

Chemicals and reagents: Amiloride hydrochloride, $CaCl_2$, $Ca(NO_3)_2$, $NaHCO_3$, $MgCl_2$ and $MgSO_4$ were from Alfa Aesar (Heysham, UK). α-chymotrypsin, gentamycin (10 mg/ml), diethyl pyrocarbonate (DEPC), glucose, NaCl, N-Methyl-D-Glucamine (NMDG), and sodium pyruvate were from Sigma Aldrich (Dorset, UK). Dimethyl sulfoxide (DMSO), 4-(2-hydroxyethyl)-1-piperazineethanesulfonic acid (HEPES) and KCl were purchased from ThermoFisher Scientific (Gloucester, UK). Stock solutions of 100 mM amiloride were made in DMSO and stored at 4

°C. Stock solutions of α-chymotrypsin (2 mg/ml) were freshly made in ORS on the day of experiments, kept on ice and used within 4 hours.

Data analysis and statistics: *Electrophysiology:* Data are presented as means ± standard error of the mean (SEM) and "n" represents the number of experiments performed. Each experimental approach was completed across 2 – 3 oocyte donors. Statistical analysis was performed using GraphPad Prism (v8.0.1; GraphPad Software Inc., San Diego, CA, USA). The D'Agostino-Pearson omnibus normality test was used to assess whether data had a Gaussian distribution. Data sets with Gaussian distribution were analysed using the two tailed Student's t-test. In addition, a Welch's correction was performed if the variances were not equal. Normally distributed multiple groups were analysed using an ordinary one-way ANOVA with post hoc Tukey's multiple comparison test. Data sets that did not follow Gaussian distribution were analysed using the two tailed Mann-Whitney U-test. A Kruskal-Wallis test with Dunn's multiple comparison test was used for the analysis of non-parametric multiple groups. Data in Figure 8 C/E were each fitted to a simple linear regression model and regression lines were compared using ANCOVA. All figures were assembled and finalised using Inkscape (v0.92.3).

Correlation of functional SCNN1D with habitat aridity: For each rodent observation, an aridity value was extracted as the median of all aridity surface values encompassed within a radius of 0.02º of the observation (approximately 2 km). To test whether gene expression explains any variation in habitat aridity, gamma error distribution (logarithmic link function) nested Generalised Linear Mixed Models (GLMM) were constructed with species within clade as nested random effects and with or without gene presence as a categorical fixed effect. Models were compared to test whether inclusion of gene presence significantly improved model fit. Analyses were conducted in R programming language (R Core Team 2019) with models constructed using the package 'lme4' (Bates et al. 2015), model comparison conducted using 'lmerTest' (Kuznetsova et al. 2017) and aridity data handled using the package 'raster' (Hijmans).

Data availability

The electrophysiology data underlying this article are available in a Zenodo depository, at https://dx.doi.org/10.5281/zenodo.5291910.

Acknowledgements

The authors thank Dr. Andreas Werner for providing *Xenopus* oocytes and Dr. Pawel Szczesniak for helpful comments on the manuscript.

Funding information

This work was supported by intramural seed grants (HOMFOR 2017-2019) by the Medical School of Saarland University (SM). MT was supported through an undergraduate summer studentship by The Physiological Society. MA receives funding from the Ministry of Culture and Science of the State of North Rhine-Westphalia (FKZ 005-2101-0144), GKC receives funding from the DFG (SFB-TR152/P22) and GVV is supported by a G0H9818N Odysseus grant from the Research Foundation Flanders (FWO).

Author Contribution

SM and MA conceived the study, SM, SMG, IR, MC, MA designed the study, SM, SMG, MC, MT, FB performed experiments, SM, SMG, IR, GVV, MC, MS, MT, MA interpreted the data and wrote the manuscript. GKC and NB provided reagents. All authors approved the manuscript.

Tables

Table 1. Presence of an open reading frame (ORF) for *SCNN1D* in currently available rodent genomes.

Rodent family	Species	Genome Assembly	*SCNN1D* ORF	Comments
Gliridae	*Muscardinus avellanarius*	MusAve_v1_BIUU	Yes	
	Glis glis	GliGli_v1_BIUU	Yes	
	Graphiurus murinus	GraMur_v1_BIUU	Yes	
Sciuridae	*Xerus inauris*[a]	XerIna_v1_BIUU	No	
	Ictidomys tridecemlineatus	SpeTri2.0	No	unsequenced parts of exon 13
	Cynomys gunnisoni	ASM1131664v1	No	
	Spermophilus dauricus	ASM240643v1	No	
	Urocitellus parryii	ASM342692v1	No	
	Marmota himalayana	ASM528016v1	No	
	Marmota marmota	marMar	No	
	Marmota monax	MONAX5	No	
Aplodontiidae	*Aplodontia rufa*	AplRuf_v1_BIUU	Yes	
Pedetidae	*Pedetes capensis*	PedCap_v1_BIUU	Yes	exon 13 information is retrieved from two different sequencing results
Anomaluridae	*No genomes available*			
Zenkerellidae	*No genomes available*			
Castoridae	*Castor canadensis*	C.can genome v1.0	Yes	invasive species
Heteromyidae	*Dipodomys ordii*	Dord_2.0	No	
Geomyidae	*No genomes available*			
Dipodidae	*Jaculus jaculus*	JacJac1.0	No	
	Allactaga bullata[b]	AllBul_v1_BIUU	No	
Zapodidae	*Zapus hudsonius*	ZapHud_v1_BIUU	Yes	
Sminthidae	*No genomes available*			
Platacanthomyidae	*No genomes available*			
Spalacidae	*Nannospalax galili*[c]	S.galili_v1.0	Yes	
Calomyscidae	*No genomes available*			
Nesomyidae	*Cricetomys gambianus*	CriGam_v1_BIUU	No	invasive species
Cricetidae	*Microtus ochrogaster*	MicOch1.0	No	
	Cricetulus barabensi griseus[d]	CriGri_1.0	No	
	Peromyscus maniculatus	Pman_1.0	No	invasive species
	Peromyscus leucopus	UCI_PerLeu_2.1	No	
	Mesocricetus auratus	MesAur1.0	No	
Muridae	*Rattus norvegicus*	Rnor_6.0	No	invasive species
	Rattus rattus	Rrattus_CSIRO_v1	No	invasive species
	Grammomys dolichurus surdaster[e]	NIH_TR_1.0	No	
	Mus musculus	GRCm39	No	invasive species
	Mus caroli	CAROLI_EIJ_v1.1	No	
	Mastomys coucha	UCSF_Mcou_1	No	
	Mus pahari	PAHARI_EIJ_v1.1	No	
Ctenodactylidae	*Ctenodactylus gundi*	CteGun_v1_BIUU	Yes	
Diatomyidae	*No genomes available*			
Hystricidae	*Hystrix cristata*	HysCri_v1_BIUU	Yes	
Bathyergidae	*Fukomys damarensis*[f]	DMR_v1.0	Yes	exon 6 yet unsequenced, remaining sequence has normal reading frame
Heterocephalidae	*Heterocephalus glaber*	HetGla_female_1.0	Yes	
Petromuridae	*Petromus typicus*	PetTyp_v1_BIUU	Yes	
Thryonomyidae	*Thryonomys swinderianus*	ThrSwi_v1_BIUU	Yes	
Erethizontidae	*Erethizon dorsatus*	GSC_porc_1.0	Yes	
Caviidae	*Dolichotis patagonum*	DolPat_v1_BIUU	No	internal stop codons
	Hydrochoerus hydrochaeris	HydHyd_v1_BIUU	Yes	
	Cavia porcellus	Cavpor3.0	Yes	invasive species
	Cavia tschudii	CavTsc_v1_BIUU	Yes	
Dasyproctidae	*Dasyprocta punctata*	DasPun_v1_BIUU	Yes	
Cuniculidae	*Cuniculus paca*	CunPac_v1_BIUU	Yes	
Chinchillidae	*Chinchilla lanigera*	ChiLan1.0	Yes	
Dinomyidae	*Dinomys branickii*	DinBra_v1_BIUU	Yes	
Abrocomidae	*No genomes available*		Yes	
Echimyidae	*Capromys pilorides*	CapPil_v1_BIUU	Yes	
	Myocastor coypus	MyoCoy_v1_BIUU	Yes	invasive species
Octodontidae	*Octodon degus*	OctDeg1.0	Yes	
Ctenomyidae	*Ctenomys sociabilis*	CteSoc_v1_BIUU	Yes	

Families that include species with intact *SCNN1D* are colour coded in blue. Light blue colour indicates *SCNN1D* without exon fusion, dark blue colour indicates *SCNN1D* with exon fusion. Magenta labels families that include species without functional *SCNN1D* (pseudogene) and red labels families in which *SCNN1D* is completely absent. Families of which genetic information is absent are labelled in grey. [a]*X. inaurus* is assigned to a subgenus, *Geosciurus inauris*. [b]*A. bullata* is assigned to a subgenus, *Orientallactaga bullata*. [c]For analysis of species distribution, the GBIF species *Spalax ehrenbergi* (a now outdated species complex) was used. [d]Observation data is also recorded as a seperate (now obsolete) species *C. griseus* in GBIF. [e]Observation data is also recorded as obsolete synonym *Thamnomys surdaster surdaster* in GBIF. [f]*F. damarensis* was previously named *Cryptomys damarensis* as recorded in GBIF (Kock et al. 2006). The species marked as invasive were excluded from the geographical and aridity analyses presented in Figure 9.

Table 2. Features of guinea pig *SCNN1* genes.

Gene	GC-content (%)	Size (bases)	GC (cDNA) (%)	GC3 (%)	Amino acids
SCNN1A	50.9	23,116	59.5	80.2	1971
SCNN1B	45.2	64,152	56.0	77.4	1926
SCNN1G	45.2	26,612	52.1	68.2	1968
SCNN1D	58.0	6,438	59.8	76.0	1740

GC-content reflects percentage of G/C bases in the respective *SCNN1* gene starting from the designated start codon towards the stop codon. GC (cDNA) reflects the overall G/C content in the coding region, GC3 the percentage of G/C in the third position of each codon. Amino acids depict the count of amino acids per *SCNN1* family member.

References

Allainé D, Rodrigue I, Berre M Le, Ramousse R. 1994. Habitat preferences of alpine marmots, Marmota marmota. *Can. J. Zool.* 72:2193–2198.

Althaus M, Bogdan R, Clauss WG, Fronius M. 2007. Mechano-sensitivity of epithelial sodium channels (ENaCs): laminar shear stress increases ion channel open probability. *FASEB J.* 21:2389–2399.

Antoine P-O, Marivaux L, Croft DA, Billet G, Ganerød M, Jaramillo C, Martin T, Orliac MJ, Tejada J, Altamirano AJ, et al. 2012. Middle Eocene rodents from Peruvian Amazonia reveal the pattern and timing of caviomorph origins and biogeography. *Proc. R. Soc. B Biol. Sci.* 279:1319–1326.

Babini E, Geisler H-S, Siba M, Gründer S. 2003. A New Subunit of the Epithelial Na+ Channel Identifies Regions Involved in Na+ Self-inhibition. *J. Biol. Chem.* 278:28418–28426.

Baines D. 2013. Kinases as Targets for ENaC Regulation. *Curr. Mol. Pharmacol.* 6:50–64.

Bates D, Mächler M, Bolker B, Walker S. 2015. Fitting Linear Mixed-Effects Models Using lme4. *J. Stat. Softw.* 67:1-48.

Bigiani A. 2020a. Salt Taste. In: The Senses: A Comprehensive Reference. Elsevier. p. 247–263.

Bigiani A. 2020b. Does ENaC Work as Sodium Taste Receptor in Humans? *Nutrients* 12:1195.

Burgin CJ, Colella JP, Kahn PL, Upham NS. 2018. How many species of mammals are there? *J. Mammal.* 99:1–14.

Chandrashekar J, Kuhn C, Oka Y, Yarmolinsky DA, Hummler E, Ryba NJP, Zuker CS. 2010. The cells and peripheral representation of sodium taste in mice. *Nature* 464:297–301.

Chang SS, Grunder S, Hanukoglu A, Rösler A, Mathew PM, Hanukoglu I, Schild L, Lu Y, Shimkets RA, Nelson-Williams C, et al. 1996. Mutations in subunits of the epithelial sodium channel cause salt wasting with hyperkalaemic acidosis, pseudohypoaldosteronism type 1. *Nat. Genet.* 12:248–253.

Chen J, Ray EC, Yates ME, Buck TM, Brodsky JL, Kinlough CL, Winarski KL, Hughey RP, Kleyman TR, Sheng S. 2015. Functional Roles of Clusters of Hydrophobic and Polar Residues in the Epithelial Na+ Channel Knuckle Domain. *J. Biol. Chem.* 290:25140–25150.

Chraïbi A, Horisberger J-D. 2002. Na Self Inhibition of Human Epithelial Na Channel. *J. Gen. Physiol.*120:133–145.

Clauss M, Hagen KB, Frei S, Ortmann S, Lawrenz A, Głogowski R, Fritz J, Flach E, Kreuzer M. 2019. Digestive anatomy, physiology, resting metabolism and methane production of captive maras (Dolichotis patagonum). *Comp. Biochem. Physiol. Part A Mol. Integr.*

Physiol. 235:82–89.

Corpet F. 1988. Multiple sequence alignment with hierarchical clustering. *Nucleic Acids Res.* 16:10881–10890.

Cox PG, Hautier L. 2015. Evolution of the Rodents. (Cox PG, Hautier L, editors.). Cambridge: Cambridge University Press

D'Elía G, Fabre P-H, Lessa EP. 2019. Rodent systematics in an age of discovery: recent advances and prospects. *J. Mammal.* 100:852–871.

Daeschler EB, Shubin NH, Jenkins FA. 2006. A Devonian tetrapod-like fish and the evolution of the tetrapod body plan. *Nature* 440:757–763.

Donald J, Pannabecker TL. 2015. Osmoregulation in Desert-Adapted Mammals. In: Sodium and Water Homeostasis. New York, NY: Springer New York.

Fabre P-H, Hautier L, Dimitrov D, P Douzery EJ. 2012. A glimpse on the pattern of rodent diversification: a phylogenetic approach. *BMC Evol. Biol.* 12:88.

Fronius M, Bogdan R, Althaus M, Morty RE, Clauss WG. 2010. Epithelial Na+ channels derived from human lung are activated by shear force. *Respir. Physiol. Neurobiol.* 170:113–119.

GBIF. 2020. GBIF.org 2020. Occurrence Download accessed 24/09/2020 https://doi.org/10.15468/dl.4ndc6p

Giraldez T, Rojas P, Jou J, Flores C, Alvarez de la Rosa D. 2012. The epithelial sodium channel δ-subunit: new notes for an old song. *Am. J. Physiol. Physiol.* 303:F328–F338.

GISD. 2020. GISD 2020. Available from: http://www.iucngisd.org/gisd/search.php

Haerteis S, Krueger B, Korbmacher C, Rauh R. 2009. The δ-Subunit of the Epithelial Sodium Channel (ENaC) Enhances Channel Activity and Alters Proteolytic ENaC Activation. *J. Biol. Chem.* 284:29024–29040.

Hanukoglu I, Hanukoglu A. 2016. Epithelial sodium channel (ENaC) family: Phylogeny, structure-function, tissue distribution, and associated inherited diseases. *Gene* 579:95-132

Hijmans RJ. raster: Geographic Data Analysis and Modeling. R package version 3.4-5. Available from: https://cran.r-project.org/package=raster

Ji H-L, Su X-F, Kedar S, Li J, Barbry P, Smith PR, Matalon S, Benos DJ. 2006. δ-Subunit Confers Novel Biophysical Features to αβγ-Human Epithelial Sodium Channel (ENaC) via a Physical Interaction. *J. Biol. Chem.* 281:8233–8241.

Kashlan OB, Blobner BM, Zuzek Z, Tolino M, Kleyman TR. 2015. Na+ Inhibits the Epithelial Na+ Channel by Binding to a Site in an Extracellular Acidic Cleft. *J. Biol. Chem.* 290:568–576.

Kleyman TR, Eaton DC. 2020. Regulating ENaC's gate. *Am. J. Physiol. Physiol.* 318:C150–C162.

Kleyman TR, Kashlan OB, Hughey RP. 2018. Epithelial Na + Channel Regulation by Extracellular and Intracellular Factors. *Annu. Rev. Physiol.* 80:263–281.

Knoepp F, Ashley Z, Barth D, Baldin J-P, Jennings M, Kazantseva M, Saw EL, Katare R, Alvarez de la Rosa D, Weissmann N, et al. 2020. Shear force sensing of epithelial Na + channel (ENaC) relies on N -glycosylated asparagines in the palm and knuckle domains of αENaC. *Proc. Natl. Acad. Sci.* 117:717–726.

Kock D, Ingram CM, Frabotta LJ, Honeycutt RL, Burda H. 2006. On the nomenclature of Bathyergidae and Fukomys n. gen. (Mammalia: Rodentia). *Zootaxa* 1142:51–55.

Kumar S, Stecher G, Li M, Knyaz C, Tamura K. 2018. MEGA X: Molecular Evolutionary Genetics Analysis across Computing Platforms.Battistuzzi FU, editor. *Mol. Biol. Evol.* 35:1547–1549.

Kuo IY, Ehrlich BE. 2012. Ion channels in renal disease. *Chem. Rev.* 112:6353–72.

Kuznetsova A, Brockhoff PB, Christensen RHB. 2017. lmerTest Package: Tests in Linear Mixed Effects Models. *J. Stat. Software* 82:1-26.

Marivaux L, Essid EM, Marzougui W, Khayati Ammar H, Adnet S, Marandat B, Merzeraud G, Tabuce R, Vianey-Liaud M. 2014. A new and primitive species of Protophiomys (Rodentia, Hystricognathi) from the late middle Eocene of Djebel el Kébar, Central Tunisia. Palaeovertebrata 38, e2.

Maxeiner S, Benseler F, Krasteva-Christ G, Brose N, Südhof TC. 2020. Evolution of the Autism-Associated Neuroligin-4 Gene Reveals Broad Erosion of Pseudoautosomal Regions in Rodents.Nowick K, editor. *Mol. Biol. Evol.* 37:1243–1258.

Mein P, Pickford M. 2006. Late Miocene micromammals from the Lukeino Formation (6.1 to 5.8 Ma), Kenya. *Bull. Mens. la Société linnéenne Lyon* 75:183–223.

Middleton N, Thomas D 1997. World atlas of desertification: Second edition. United Nations Environment Programme.

Molloy SS, Bresnahan PA, Leppla SH, Klimpel KR, Thomas G. 1992. Human furin is a calcium-dependent serine endoprotease that recognizes the sequence Arg-X-X-Arg and efficiently cleaves anthrax toxin protective antigen. *J. Biol. Chem.* 267:16396–16402.

Nie H-G, Chen L, Han D-Y, Li J, Song W-F, Wei S-P, Fang X-H, Gu X, Matalon S, Ji H-L. 2009. Regulation of epithelial sodium channels by cGMP/PKGII. *J. Physiol.* 587:2663–2676.

Nomura K, Nakanishi M, Ishidate F, Iwata K, Taruno A. 2020. All-Electrical Ca2+-Independent Signal Transduction Mediates Attractive Sodium Taste in Taste Buds. *Neuron* 106:816-829.e6.

Noreng S, Bharadwaj A, Posert R, Yoshioka C, Baconguis I. 2018. Structure of the human epithelial sodium channel by cryo-electron microscopy. *Elife* 7.

Noreng S, Posert R, Bharadwaj A, Houser A, Baconguis I. 2020. Molecular principles of

assembly, activation, and inhibition in epithelial sodium channel. *Elife* 9.

Palmer LG, Schnermann J. 2015. Integrated Control of Na Transport along the Nephron. *Clin. J. Am. Soc. Nephrol.* 10:676–687.

Patterson BD, Upham NS. 2014. A newly recognized family from the Horn of Africa, the Heterocephalidae (Rodentia: Ctenohystrica). *Zool. J. Linn. Soc.* 172:942–963.

Paudel P, McDonald F, Fronius M. 2021. The δ subunit of epithelial sodium channel in humans - a potential player in vascular physiology. *Am. J. Physio. Heart. Circ. Physiol.* 320:H487-H493

Polly PD. 2003. Paleophylogeography: The tempo of geographic differentiation in marmots (Marmota). *J. Mammal.* 84:369–384.

R Core Team. 2019. R: A language and environment for statistical computing. *R Found. Stat. Comput.* Vienna, Austria. https://www.R-project.org/.

Rossier BC, Baker ME, Studer RA. 2015. Epithelial Sodium Transport and Its Control by Aldosterone: The Story of Our Internal Environment Revisited. *Physiol. Rev.* 95:297–340.

Saxena A, Hanukoglu I, Strautnieks SS, Thompson RJ, Gardiner RM, Hanukoglu A. 1998. Gene structure of the human amiloride-sensitive epithelial sodium channel beta subunit. *Biochem. Biophys. Res. Commun.* 252:208-213.

Schild L. 2010. The epithelial sodium channel and the control of sodium balance. *Biochim. Biophys. Acta - Mol. Basis Dis.* 1802:1159–1165.

Sheng S, Carattino MD, Bruns JB, Hughey RP, Kleyman TR. 2006. Furin cleavage activates the epithelial Na + channel by relieving Na + self-inhibition. *Am. J. Physiol. Physiol.* 290:F1488–F1496.

Shimkets RA, Warnock DG, Bositis CM, Nelson-Williams C, Hansson JH, Schambelan M, Gill JR, Ulick S, Milora R V., Findling JW, et al. 1994. Liddle's syndrome: Heritable human hypertension caused by mutations in the β subunit of the epithelial sodium channel. *Cell* 79:407–414.

Steppan SJ, Storz BL, Hoffmann RS. 2004. Nuclear DNA phylogeny of the squirrels (Mammalia: Rodentia) and the evolution of arboreality from c-myc and RAG1. *Mol. Phylogenet. Evol.* 30:703–719.

Trabucco A, Zomer RJ. 2018. Global Aridity Index and Potential Evapotranspiration (ET0) Climate Database v2. *CGIAR Consort. Spat. Inf.* Published online, available from the CGIAR-CSI GeoPortal at https://cgiarcsi.community

Waldmann R, Champigny G, Bassilana F, Voilley N, Lazdunski M. 1995. Molecular Cloning and Functional Expression of a Novel Amiloride-sensitive Na+ Channel. *J. Biol. Chem.* 270:27411–27414.

Weers DJ Van. 2005. A taxonomic revision of the Pleistocene Hystrix (Hystricidae, Rodentia)

from Eurasia with notes on the evolution of the family. *Contrib. to Zool. (Amsterdam)* 74:301-312.

Wesch D, Althaus M, Miranda P, Cruz-Muros I, Fronius M, González-Hernández T, Clauss WG, Alvarez de la Rosa D, Giraldez T. 2012. Differential N termini in epithelial Na + channel δ-subunit isoforms modulate channel trafficking to the membrane. *Am. J. Physiol. Physiol.* 302:C868–C879.

Wichmann L, Althaus M. 2020. Evolution of epithelial sodium channels: current concepts and hypotheses. *Am. J. Physiol. Integr. Comp. Physiol.* 319:R387–R400.

Wichmann L, Dulai JS, Marles-Wright J, Maxeiner S, Szczesniak PP, Manzini I, Althaus M. 2019. An extracellular acidic cleft confers profound H+-sensitivity to epithelial sodium channels containing the δ-subunit in Xenopus laevis. *J. Biol. Chem.* 294:12507–12520.

Wichmann L, Vowinkel KS, Perniss A, Manzini I, Althaus M. 2018. Incorporation of the δ-subunit into the epithelial sodium channel (ENaC) generates protease-resistant ENaCs in Xenopus laevis. *J. Biol. Chem.* 293:6647–6658.

Wilson DE, Lacher TE, Mittermeier RA. 2016. Handbook of the mammals of the World. Vol. 6 Lagomorphs and Rodents I. IBarcelona: Lynx Edition.

Wilson DE, Lacher TE, Mittermeier RA. 2017. Handbook of the Mammals of the World. Volume 7: Rodents II. Barcelona: Lynx Edition.

Wu H, Guang X, Al-Fageeh MB, Cao J, Pan S, Zhou H, Zhang L, Abutarboush MH, Xing Y, Xie Z, et al. 2014. Camelid genomes reveal evolution and adaptation to desert environments. *Nat. Commun.* 5:5188.

Zhang J, Li S, Deng F, Baikeli B, Yu W, Liu G. 2019. Distribution of aquaporins and sodium transporters in the gastrointestinal tract of a desert hare, Lepus yarkandensis. *Sci. Rep.* 9:16639.

Zhao R-Z, Nie H-G, Su X-F, Han D-Y, Lee A, Huang Y, Chang Y, Matalon S, Ji H-L. 2012. Characterization of a novel splice variant of δ ENaC subunit in human lungs. *Am. J. Physiol. Cell. Mol. Physiol.* 302:L1262–L1272.

Figure 1

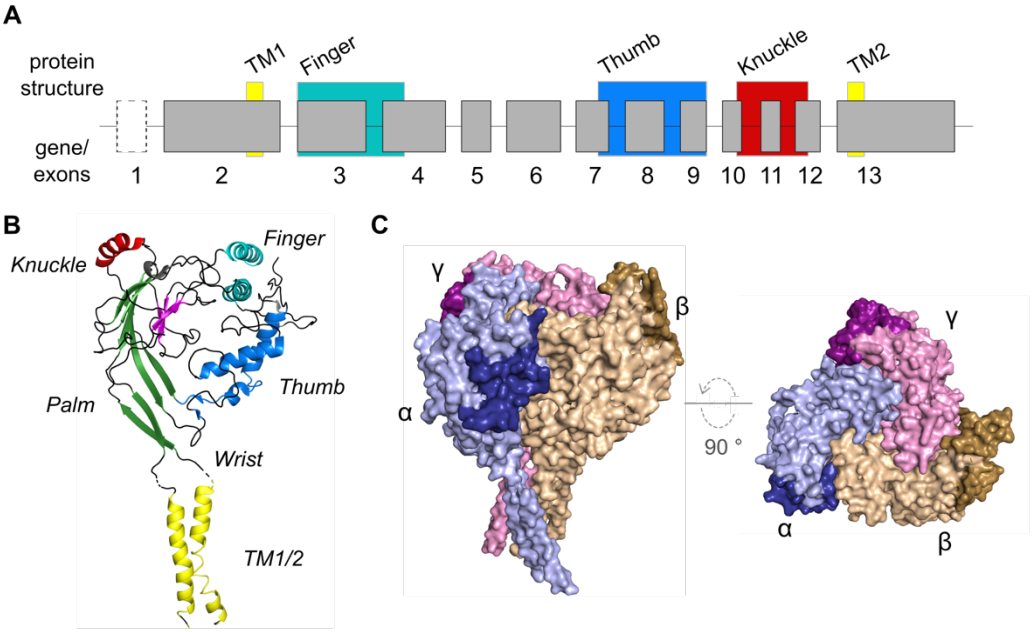

Figure 1. Proposed nomenclature of *SCNN1* genes and structural features of the human αβγ-ENaC. A) The *SCNN1 genes* share a canonical organization in which the coding DNA is distributed over at least twelve exons (exon 2 to 13). Due to the high variability of exon 2, different predicted start codons located on alternative exons preceding exon 2 as well as the absence of a likely start codon on exon 2 in certain species, make an additional exon(-s) necessary and are therefore depicted in a dashed box. Structural features obtained from the cryo-EM-derived structure of human αβγ-ENaC were imposed to the respective encoding exons. All structural features are highlighted with coloured boxes. Only exon sizes and not intron sizes are drawn to scale. **B)** SCNN1 proteins share an overall hand-like structure, including regions representing 'finger', 'thumb', 'palm', 'wrist' and 'knuckle', holding a 'ball of β-sheets' (shown in magenta). Transmembrane regions are termed TM1 and TM2. The image shows the human ENaC α-subunit (Noreng et al. 2018). **C)** Surface model of the cryo-EM-derived structure of human αβγ-ENaC (Noreng et al. 2018). Gating Relief of Inhibition by Proteolysis (GRIP) domains are highlighted in darker colours.

Figure 2

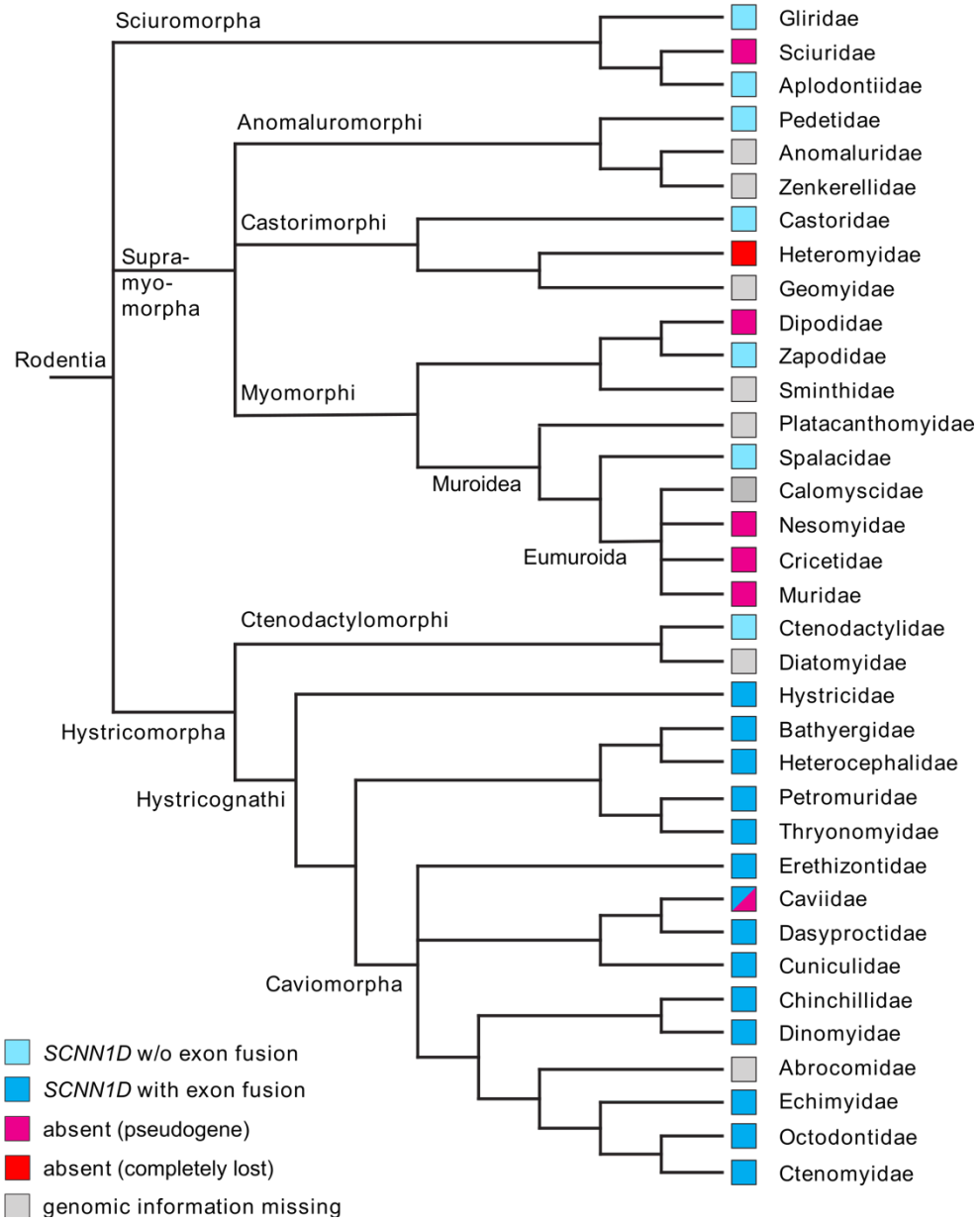

Figure 2. Presence of *SCNN1D* in rodent families. Families marked in magenta include species which lost a functional *SCNN1D,* i.e. families with pseudogene versions of *SCNN1D*. *SCNN1D* is completely absent in the Heteromyidae marked in red. All families marked in blue maintained intact *SCNN1D* genes. Families highlighted in dark blue contain species in which exons 11 and 12 of *SCNN1D* are fused to a 'super-exon', whereas light blue families do not include species with *SCNN1D* exon fusion (w/o = without exon fusion). There is currently no available genomic information of species representing the families highlighted in grey. Note that the Caviidae family contains species with and without intact *SCNN1D*. A list of all species that were analysed is provided in Table 1. The classification of rodents into 35 families is based on D'Elía et al. (2019), the taxon Eumuroida was suggested by Steppan et al. (2004).

Figure 3

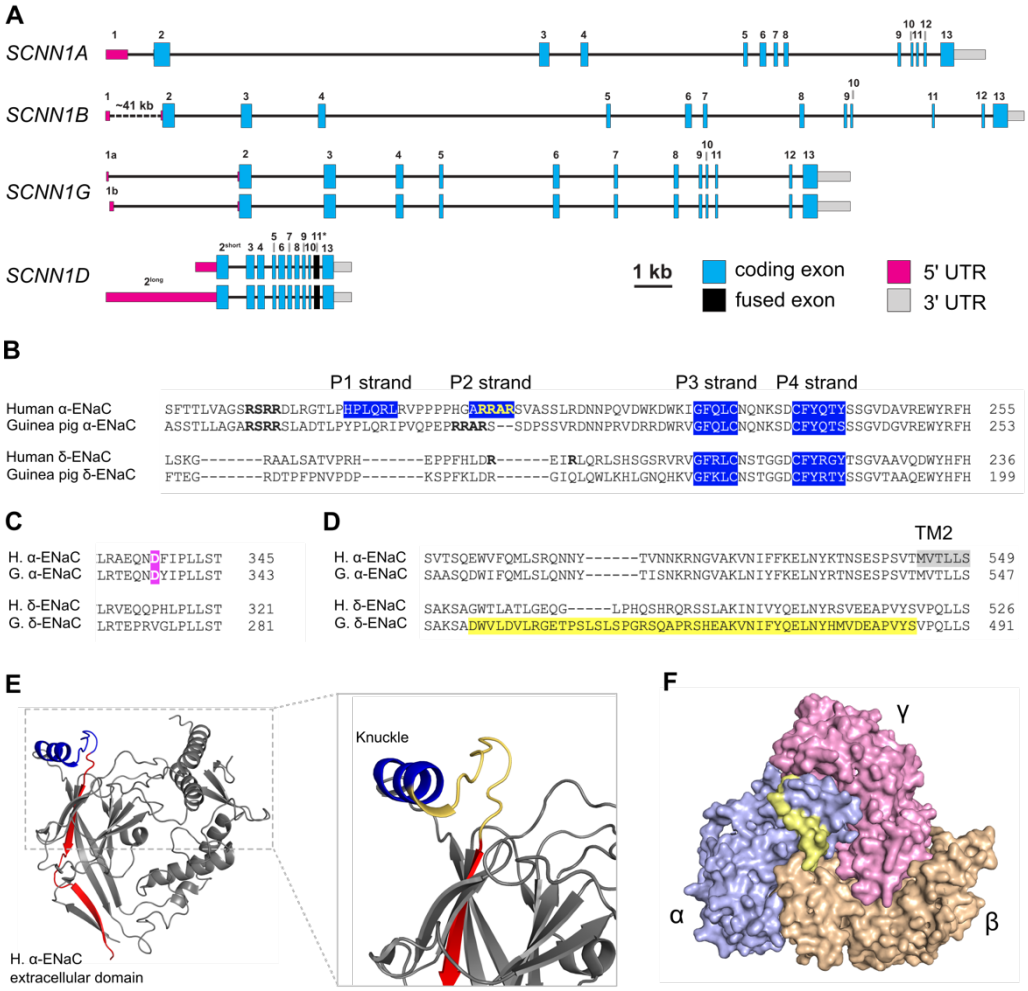

Figure 3. Genomic organisation and peptide sequences of guinea pig *SCNN1D*. A) All *SCNN1* family members are depicted relative to scale with the exception of an intron following *SCNN1B* exon 1, which is located roughly 41 kb upstream of *SCNN1B* exon 2. Blue boxes represent coding regions, grey boxes represent 3'UTR, i.e., sequences immediately downstream of the respective stop codons to the first poly-adenylation sequence motif. 5'RACE analyses encompass exon/exon junctions and resulted in 5'UTR sequence information depicted in magenta. This is reflected in either alternative exons upstream of *SCNN1G* (exon 1a and 1b) or alternative transcriptional start sites of *SCNN1D* formally lacking any upstream exon. The fusion of exon 11 and exon 12 to a 'super-exon' 11* is depicted in black. **B)** Alignment of the amino acid sequences of the extracellular GRIP domains, based on Noreng et al. (2020), of human and guinea pig α- and δ-ENaC. Consensus sites for the protease furin are highlighted in bold letters. P1 to P4 strands of the Gating Relief of Inhibition by Proteolysis (GRIP) domains are highlighted in blue. **C)** Alignment of amino acid sequences that are part of the extracellular acidic cleft with the putative sodium coordination sites (Asp-338 in human α-ENaC) highlighted in magenta. **D)** Alignment of amino acid sequences close to the beginning of the second transmembrane domain (TM2) with the 'super-exon' 11* of guinea pig δ-ENaC highlighted in yellow. A full sequence alignment is provided in Supplemental Data 2. **E)** The region coded by exons 11 (blue) and 12 (red) are highlighted in the structure of the extracellular domain of the human ENaC α-subunit (Noreng et al. 2020). The magnification shows the region between Gln-509 and Ala-522 of the knuckle domain in yellow. This corresponds to the region of incorporated amino acids in guinea pig δ-ENaC due to exon fusion. **F)** Surface representation of the extracellular domain of human αβγ-ENaC, highlighting the presence of the region between Q509 and A522 in yellow at the protein surface.

Figure 4

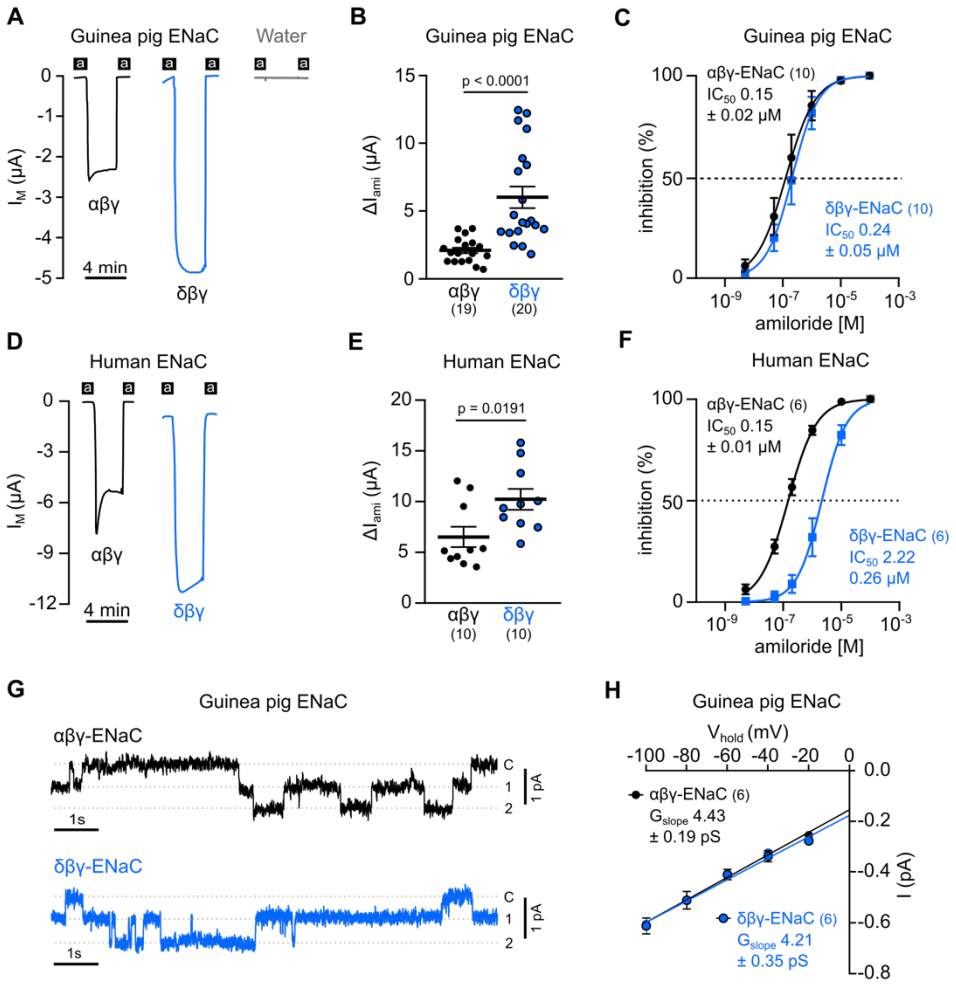

Figure 4. Guinea pig δβγ-ENaC forms a functional channel when expressed in *Xenopus* oocytes. A) Transmembrane current (I_M) traces of oocytes expressing guinea pig αβγ- and δβγ-ENaC as well as water-injected control oocytes at -60 mV holding potential. Application of 100 μM amiloride is represented by black bars (a). **B)** Amiloride-sensitive current fractions (ΔI_{ami}) for guinea pig αβγ- and δβγ-ENaCs (Student's unpaired t-test with Welch's correction). **C)** Amiloride IC_{50} values were determined from concentration-response experiments for guinea pig αβγ- (black) and δβγ-ENaC (blue). **D)** Representative I_M traces of oocytes expressing human αβγ- and δβγ-ENaC at -60 mV holding potential. **E)** ΔI_{ami} for human αβγ- and δβγ-ENaC (Student's unpaired t-test). **F)** Amiloride IC_{50} values for human αβγ- (black) and δβγ-ENaC (grey) as determined from concentration-response experiments. **G)** Representative current traces of guinea pig αβγ- and δβγ-ENaC expressing oocytes from cell-attached patch-clamp recordings at a holding potential of -100 mV (c = closed; 1-2, number of open channels). **H)** Slope conductance (G_{slope}) of guinea pig αβγ- and δβγ-ENaC, derived from linear regression of unitary channel conductance at holding potentials between -100 mV to -20 mV. Numbers in parentheses indicate (n).

Figure 5

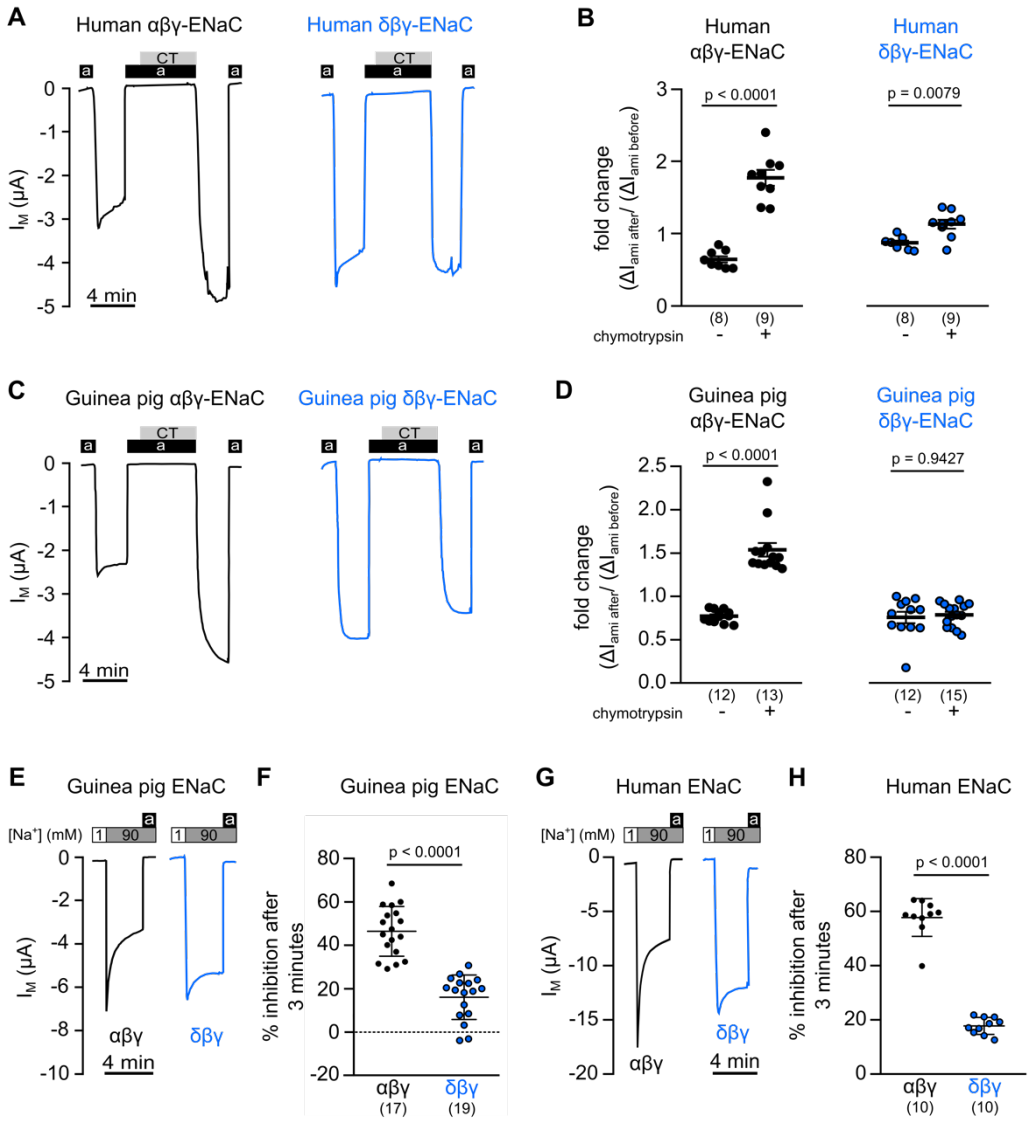

Figure 5. Isoform-specific control of ENaC activity by proteases and sodium. A) Representative transmembrane current (I_M) traces of human αβγ- and δβγ-ENaC expressing oocytes, showing the determination of amiloride-sensitive fractions of I_M (ΔI_{ami}) before and after application of chymotrypsin (2 µg/ml, CT, grey bar) with amiloride (100 µM, a, black bar). **B)** ΔI_{ami} were calculated as the difference between I_M at 3 min after wash-out of amiloride and the I_M under subsequent presence of amiloride. The fold change (ΔI_{ami} after chymotrypsin / ΔI_{ami} before chymotrypsin) is shown for human αβγ- and δβγ-ENaC expressing oocytes that were exposed to chymotrypsin as shown in panel A, in comparison with identical control experiments without chymotrypsin (Student's paired t-test). **C and D)** Data from experiments with guinea pig ENaC expressing oocytes that were identical to those shown in panels A and B. Statistical analysis shown in panel D was performed with a Mann-Whitney U-test. **E)** Representative I_M trace showing sodium self-inhibition of guinea pig αβγ- and δβγ-ENaC expressing oocytes. Application of amiloride is represented by black bars (a) and $[Na^+]$ is represented by white (90 mM) and grey (1 mM) bars. The perfusion was at a fast speed of 12 ml/min. **F)** The percentage of SSI is shown for guinea pig αβγ- and δβγ-ENaC (Student's unpaired t-test). SSI was calculated as ((ΔI_M peak – ΔI_M 3min)/ ΔI_M peak) x 100), where ΔI_M peak = initial I_M under 1 mM $[Na^+]$ – peak I_M under 90 mM $[Na^+]$, and ΔI_M after 3 min = initial I_M under 1 mM $[Na^+]$ – I_M after 3 minutes under 90 mM $[Na^+]$. **G and H)** Data obtained from experiments using human αβγ- and δβγ-ENaC expressing oocytes. Experiments were identical to those shown in panels E and F. Statistical analysis of data shown in panel F was performed using a Student's unpaired t-test with Welch's correction. Numbers in parentheses indicate (n).

Figure 6

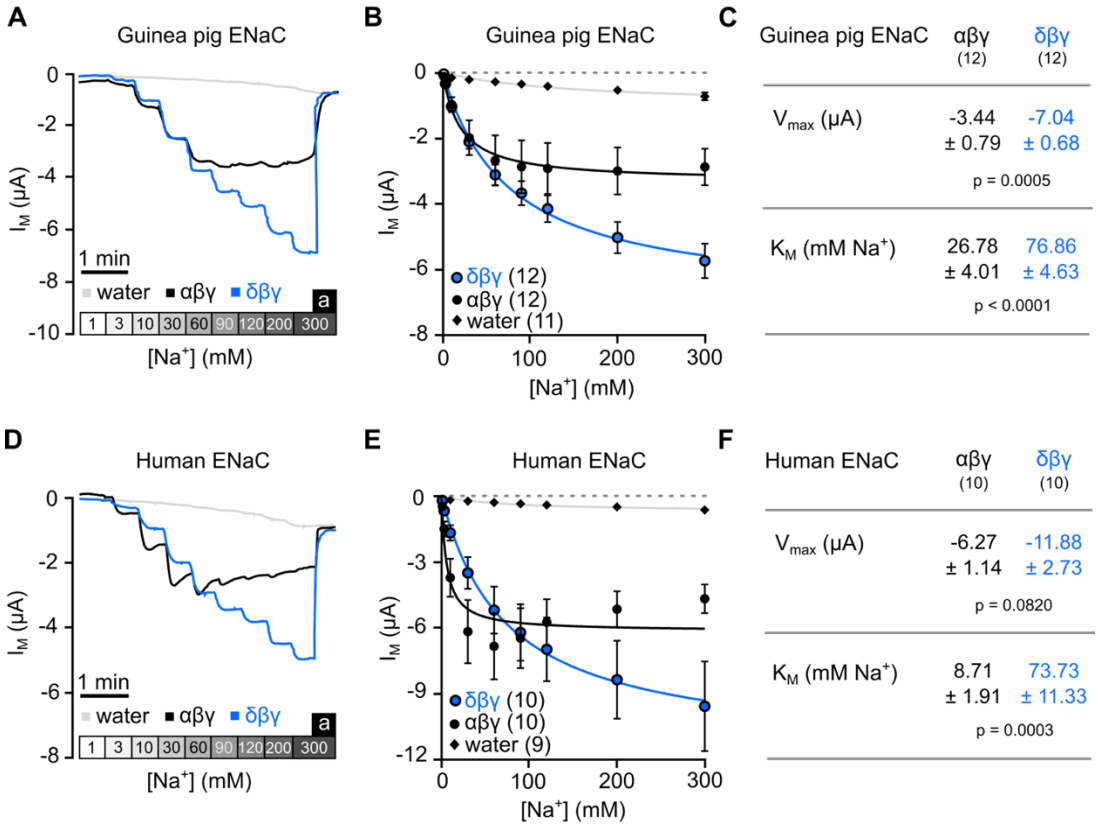

Figure 6. Both human and guinea pig δβγ-ENaC have increased activity compared to αβγ-ENaC at high extracellular Na^+ concentrations. A) Representative transmembrane current (I_M) traces for guinea pig αβγ- and δβγ-ENaC expressing oocytes as well as water-injected control oocytes. Boxes shaded in grey represent the different extracellular [Na^+] in mM. **B)** The I_M values of guinea pig ENaC expressing oocytes were plotted against the extracellular [Na^+] and fitted to the Michaelis-Menten equation allowing the estimation of V_{max} and the K_M. **C)** The V_{max} values and K_M values of guinea pig αβγ- and δβγ-ENaC expressing oocytes (Mann-Whitney U-test). **D – F)** Similar to A – C except for oocytes expressing human ENaC orthologues and separate water-injected control oocytes. Data shown in panel F were statistically analysed with Student's unpaired t-test with Welch's correction. Numbers in parentheses indicate (n).

Figure 7

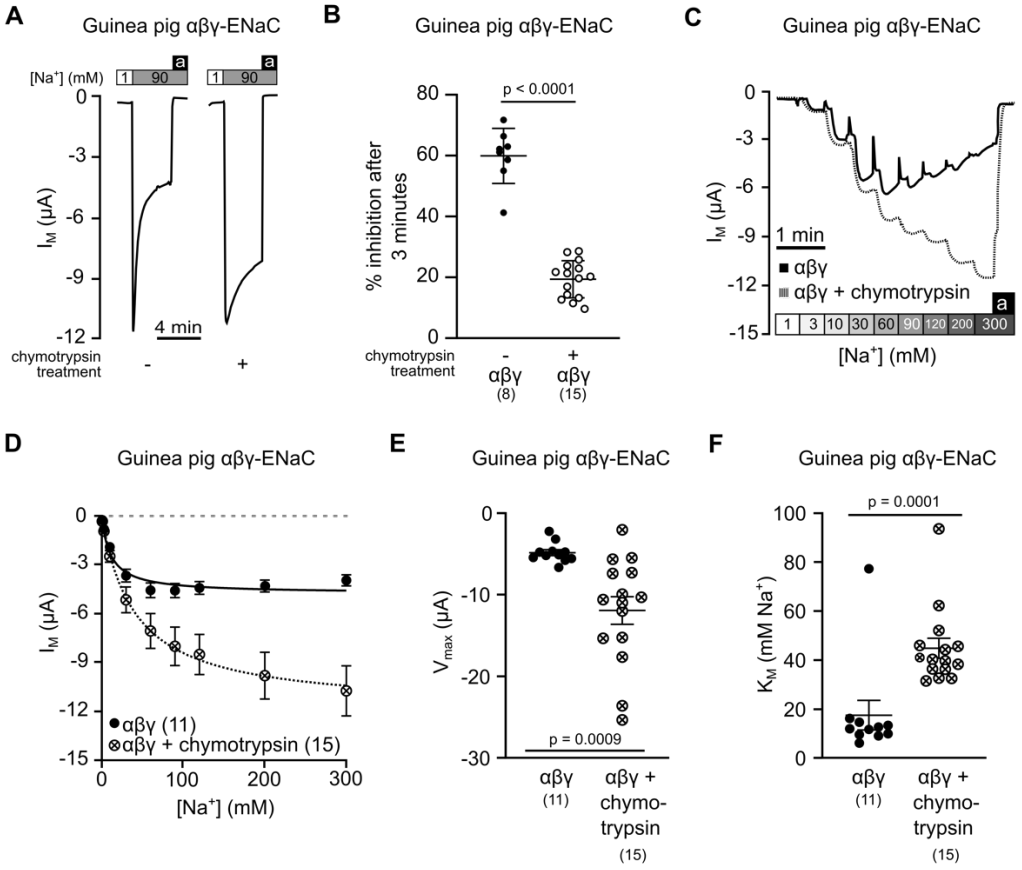

Figure 7. Reduced sodium self-inhibition is pivotal to ENaC activity at high extracellular Na^+ concentrations. A) Representative transmembrane current (I_M) traces showing sodium self-inhibition (SSI), determined with guinea pig αβγ-ENaC expressing oocytes, with and without prior incubation with chymotrypsin (2 μg/ml in NMDG-ORS for 5 minutes). Application of amiloride (100 μM) is represented by black bars (a) and [Na^+] is represented by white (90 mM) and grey (1 mM) bars. The perfusion speed was 12 ml/min. **B)** The percentage of SSI was plotted for guinea pig αβγ-ENaC with and without prior incubation with chymotrypsin (Student's unpaired t-test). SSI was calculated as ((ΔI_M peak – ΔI_M 3min)/ ΔI_M peak) x 100), where ΔI_M peak = initial I_M under 1 mM [Na^+] – peak I_M under 90 mM [Na^+], and ΔI_M after 3 min = initial I_M under 1 mM [Na^+] – I_M after 3 minutes under 90 mM [Na^+]. **C)** Representative I_M traces for guinea pig αβγ-ENaC expressing oocytes with and without prior incubation with chymotrypsin (2 μg/ml for 5 minutes) across a range of extracellular Na^+ concentrations ([Na^+]), grey shaded boxes). **D)** The I_M from experiments shown in panel C were plotted against the extracellular [Na^+] and fitted to the Michaelis-Menten equation allowing the estimation of the maximum I_M (V_{max}) and the [Na^+] at which half of V_{max} is reached (K_M). **E)** The V_{max} values of guinea pig αβγ-ENaC with and without prior incubation with chymotrypsin (Student's unpaired t-test with Welch's correction). **F)** The K_M values of guinea pig αβγ-ENaC with and without prior incubation with chymotrypsin (Mann-Whitney U-test). Numbers in parentheses indicate (n).

Figure 8

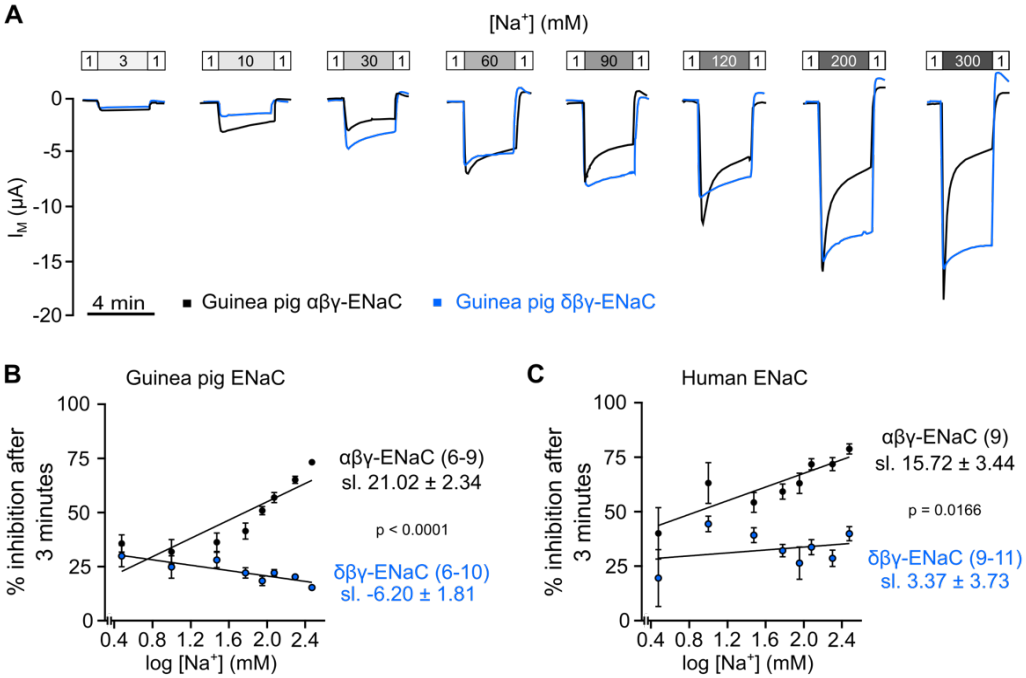

Figure 8. The reduced sodium self-inhibition of human and guinea pig δβγ-ENaC generates increased activity at high extracellular Na^+ concentrations. A) Representative transmembrane current (I_M) traces of guinea pig αβγ- and δβγ-ENaC at different extracellular Na^+ concentrations ($[Na^+]$). Recordings of a given extracellular $[Na^+]$ were performed in individual oocytes. The perfusion speed was 16 ml/min. **B and C)** The percentage of sodium self-inhibition for guinea pig and human ENaC expressing oocytes plotted against logarithmic transformations of concentrations of extracellular $[Na^+]$. SSI was calculated as ((ΔI_M peak – ΔI_M 3min)/ ΔI_M peak) x 100), where ΔI_M peak = initial I_M under 1 mM $[Na^+]$ – peak I_M under 90 mM $[Na^+]$, and ΔI_M after 3 min = initial I_M under 1 mM $[Na^+]$ – I_M after 3 minutes under 90 mM $[Na^+]$. Slopes (sl.) were derived from linear regressions and p-values, derived from ANCOVA, demonstrate the difference between slopes. Numbers in parentheses indicate (n).

Figure 9

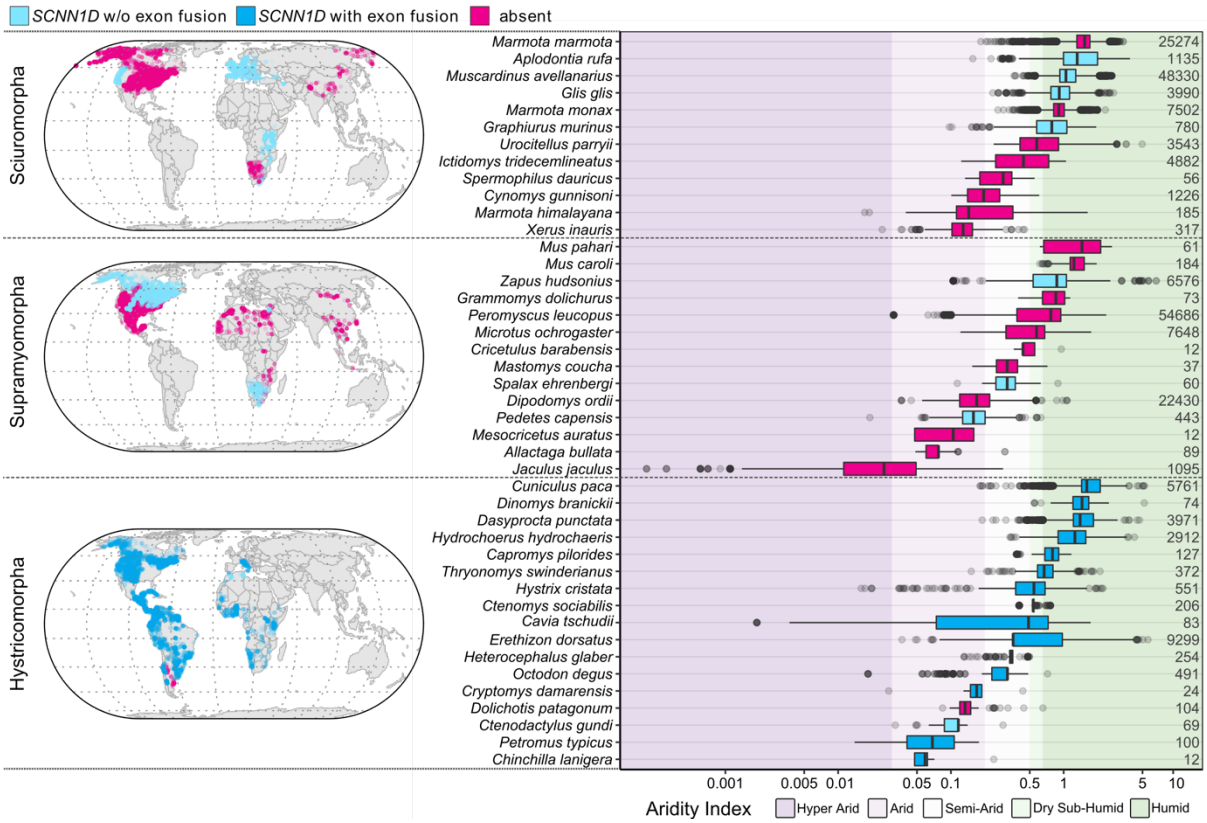

Figure 9. The loss of *SCNN1D* does not generally correlate with habitat aridity. Geolocation data of the rodent species listed in Table 1 were extracted from the Global Biodiversity Information Facility (GBIF) and were used to plot the global distribution of non-invasive rodent species of the clades Sciuromorpha, Supramyomorpha and Hystricomorpha. Global distribution of individual species is provided in Supplemental Figures 2-5. Observations for the indicated species were also plotted with corresponding habitat aridity. Mixed effects models suggest that the absence or presence of functional *SCNN1D* in the investigated species does not explain any significant proportion variation in habitat aridity. The colours indicate absence or presence of functional *SCNN1D*: Light blue = *SCNN1D* without exon fusion; Dark blue = *SCNN1D* with exon fusion; Magenta = species without functional *SCNN1D* (pseudogene and complete gene loss). Background colours differentiate habitats following the generalised climate classification scheme for aridity index values (Middleton and Thomas 1997). Species are ordered based on ascending median aridity within each clade. The numbers to the right of the plots indicate the number of GBIF observations that were extracted for each species.